nature microbiology

Article

https://doi.org/10.1038/s41564-025-02201-6

Transcription co-inhibition alters drug resistance evolution and enhances *Mycobacterium tuberculosis* clearance from granulomas

Received: 14 February 2025

Accepted: 22 October 2025

Published online: 03 December 2025

Check for updates

Barbara Bosch[1,8] ✉, Vanisha Munsamy-Govender[2,8], Jansy Sarathy[3,4], Mirjana Lilic[1], Paul Dominic B. Olinares[5], Kathryn A. Eckartt[2], Pranav Nalam[1], Markus Lang[6], Marcell Simon[1,7], Adrian Richter[6], Jeremy M. Rock[2,9] ✉ & Elizabeth A. Campbell[1,9] ✉

Mycobacterium tuberculosis (Mtb), the causative agent of tuberculosis, remains the deadliest human pathogen. Treatment is hampered by drug resistance and the persistence of slow-growing or non-replicating populations. Rifampicin, a cornerstone of first-line therapy, inhibits transcription during promoter escape, but resistance mutations undermine efficacy and drive resistance spread. We revisited the transcription cycle as an antibacterial target by characterizing AAP-SO_2, an RNA polymerase inhibitor with whole-cell activity against Mtb. AAP-SO_2 slows the nucleotide addition cycle, disrupting elongation and termination. Rifampicin-resistant mutations impose fitness costs by perturbing the balance of these steps, creating exploitable weaknesses. Inhibition of transcription with AAP-SO_2 reduced the evolution of rifampicin resistance and was especially effective against the most common resistant mutant. Combination treatment with rifampicin and AAP-SO_2 synergistically killed non-replicating Mtb in an ex vivo rabbit granuloma model. These findings show that exploiting functional vulnerabilities of the transcription cycle can counter rifampicin resistance and improve clearance of recalcitrant Mtb populations.

Tuberculosis (TB) is the deadliest infectious disease globally, with ~1.25 million deaths in 2023[1]. In addition, ~25% of the world's population (~1.7 billion people) is estimated by the World Health Organization to have been infected with *Mycobacterium tuberculosis* (Mtb) and the Centers for Disease Control and Prevention treat such cases as latent TB infections (LTBIs)[2,3]. Efforts to eradicate TB are hindered by drug resistance and the challenges associated with treating slow-growing or non-replicating Mtb, especially in the context of pulmonary necrotic granulomas[4–6].

TB treatment relies on combination therapy to both shorten treatment duration and limit drug resistance[7]. The first-line regimen includes four drugs: rifampicin (Rif), isoniazid, ethambutol (EMB) and pyrazinamide. Rif, which inhibits RNA polymerase (RNAP), is the cornerstone drug in the regimen. It is especially important for sterilizing slow-growing or non-replicating bacteria, such as those found in granulomas[8]. LTBIs are treated with either a combination of Rif (or the Rif derivative, rifapentine) and isoniazid for 3 months or Rif alone for 4–6 months[9,10].

Due to Rif's central role in TB therapy, Rif resistance is a serious concern[11]. In 2023[1], there were ~400,000 cases of Rif-resistant TB, which made up about one-fifth of all deaths due to antibiotic resistance[12]. The most common Rif-resistant mutation is a serine-to-leucine substitution

A full list of affiliations appears at the end of the paper. ✉e-mail: bbosch@rockefeller.edu; rock@rockefeller.edu; campbee@rockefeller.edu

https://doi.org/10.1038/s41564-025-02201-6

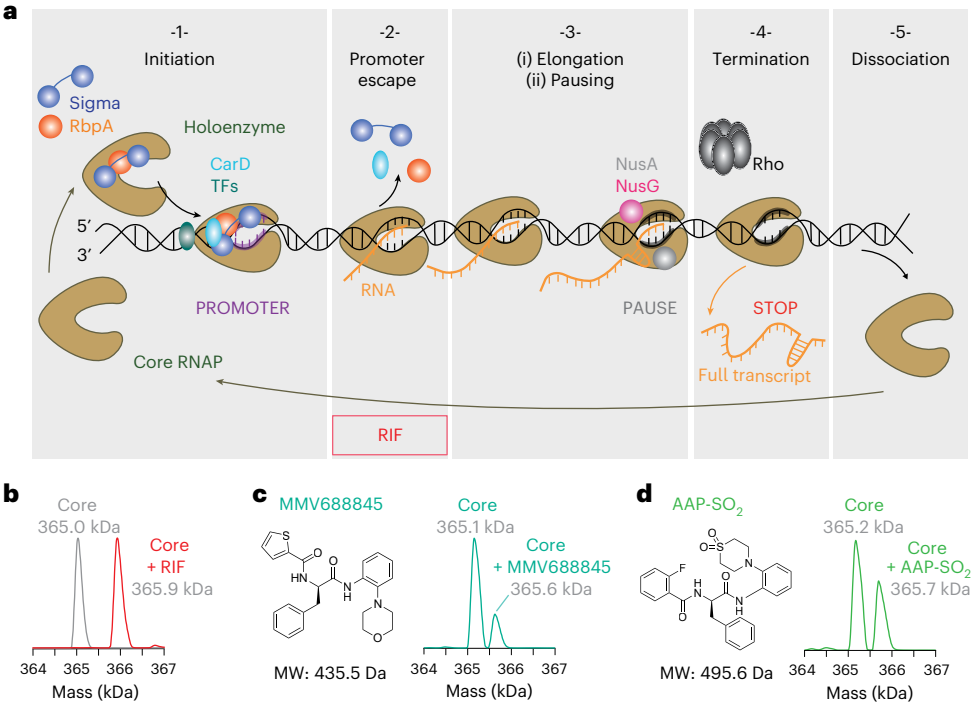

Fig. 1 | The Mtb transcription cycle consists of multiple steps for targeted inhibition. a, The bacterial transcription cycle involves five general steps: initiation, promoter escape, elongation/pausing, termination and core dissociation. Rif, the only antitubercular therapy targeting transcription, inhibits the promoter escape step. **b**, Native mass spectrometry analysis of Mtb RNAP core (grey spectrum) with measured mass consistent with the correct subunit stoichiometry (α2ββ′ω). Incubation of the RNAP core with Rif (823 Da) (red spectrum) completely shifted the peak from core to the Rif-bound complex. **c**,**d**, Native mass spectrometry analysis of RNAP core incubated with MMV688845 (436 Da) (aquamarine spectrum) or AAP-SO_2 (496 Da) (green spectrum) showed peak shifts corresponding to their respective masses, validating these compounds as RNAP binders. Detailed mass analyses can be found in Extended Data Fig. 1.

in the RNAP β subunit (βS450L), which leads to loss of Rif binding[13–16]. To treat Rif-resistant TB, BPaL (bedaquiline, pretomanid and linezolid) has recently been approved but its use requires caution due to the rapid evolution of drug resistance[17,18]. These challenges highlight the need for innovative combination therapies targeting both drug-sensitive and drug-resistant TB.

Given RNAP's essential function and vulnerability in Mtb[19], we investigated whether targeting distinct steps of the transcription cycle could enhance treatment efficacy. The transcription cycle (Fig. 1a) is a highly regulated, multistep process that includes: (1) initiation, where promoter recognition and DNA melting occur; (2) promoter escape, where RNAP breaks free from promoter-specific interactions; (3) elongation, where RNA synthesis proceeds, modulated by pausing; (4) termination, where RNA is released from the DNA template and RNAP; and (5) dissociation, where RNAP detaches from the DNA to restart the cycle[20–25]. All the steps of the transcription cycle are potential antibiotic targets. Importantly, pausing and termination are kinetically competitive with elongation, meaning that changes in the rates of elongation inversely affect the rates of pausing and termination[26].

Currently, two RNAP inhibitors with activity against early transcription steps are clinically available. Fidaxomicin (Fdx), used to treat the intestinal pathogen *Clostridioides difficile*, inhibits initiation by preventing RNAP clamp closure on DNA[27–29]. Fdx is not used for TB due to low bioavailability. The second inhibitor is Rif, which blocks promoter escape by obstructing nascent transcript translocation, leading to abortive transcripts[15,30].

To explore alternative ways to inhibit transcription, we revisited the transcription cycle as a target by exploring the RNAP inhibitor AAP-SO_2 (refs. 31–33), an *N*α-aroyl-*N*-aryl-phenylalanine amide (AAP)[33]. AAP-SO_2, an analogue of the antimycobacterial compound MMV688845, exhibits whole-cell activity against Mtb and related species[34,35]. AAP-SO_2 is chemically related to D-AAP1 (ref. 36), hypothesized to target elongation due to its binding site overlapping with CumBRe Inc's *N*-hydroxy-*N*′-phenyl-3-trifluoromethyl-benzamidine (CBR) compounds that inhibit *Escherichia coli* (*E. coli*) RNAP. CBR compounds work by inhibiting RNAP elongation and increasing rates of pausing[37–39].

Previous studies linked the βS450L mutation's fitness cost to slow elongation and hypertermination[13,14]. An elongation inhibitor would exacerbate the functional vulnerability of βS450L RNAP, further increasing its fitness cost relative to Rif-sensitive (RifS) strains. Our findings revealed that AAP-SO_2 slows nucleotide addition during elongation and profoundly increases rates of termination. We then uncovered the biochemical and structural basis of the increased potency of AAP-SO_2 over the original AAP compounds. Furthermore, we demonstrated that AAP-SO_2 minimizes the emergence of Rif resistance and specifically limits the evolution of βS450L Rif resistance in Mtb. We also found that AAP-SO_2 effectively sterilizes βS450L Rif-resistant Mtb in time-kill experiments. Importantly, the combination of Rif with AAP-SO_2 showed synergistic killing of non-replicating Mtb in an ex vivo caseum model.

Taken together, these results underscore the potential of a rational drug combination approach that dually targets the RNAP—critical for the survival of both replicating and non-replicating Mtb—to increase treatment efficacy and slow the evolution of drug resistance.

Results

A pipeline to evaluate direct target engagement of putative Mtb RNAP inhibitors

To confirm the mode of action and to determine the structural basis of the increased potency of the inhibitor AAP-SO_2 over the parent compounds[31], we first required evidence of direct target engagement

https://doi.org/10.1038/s41564-025-02201-6

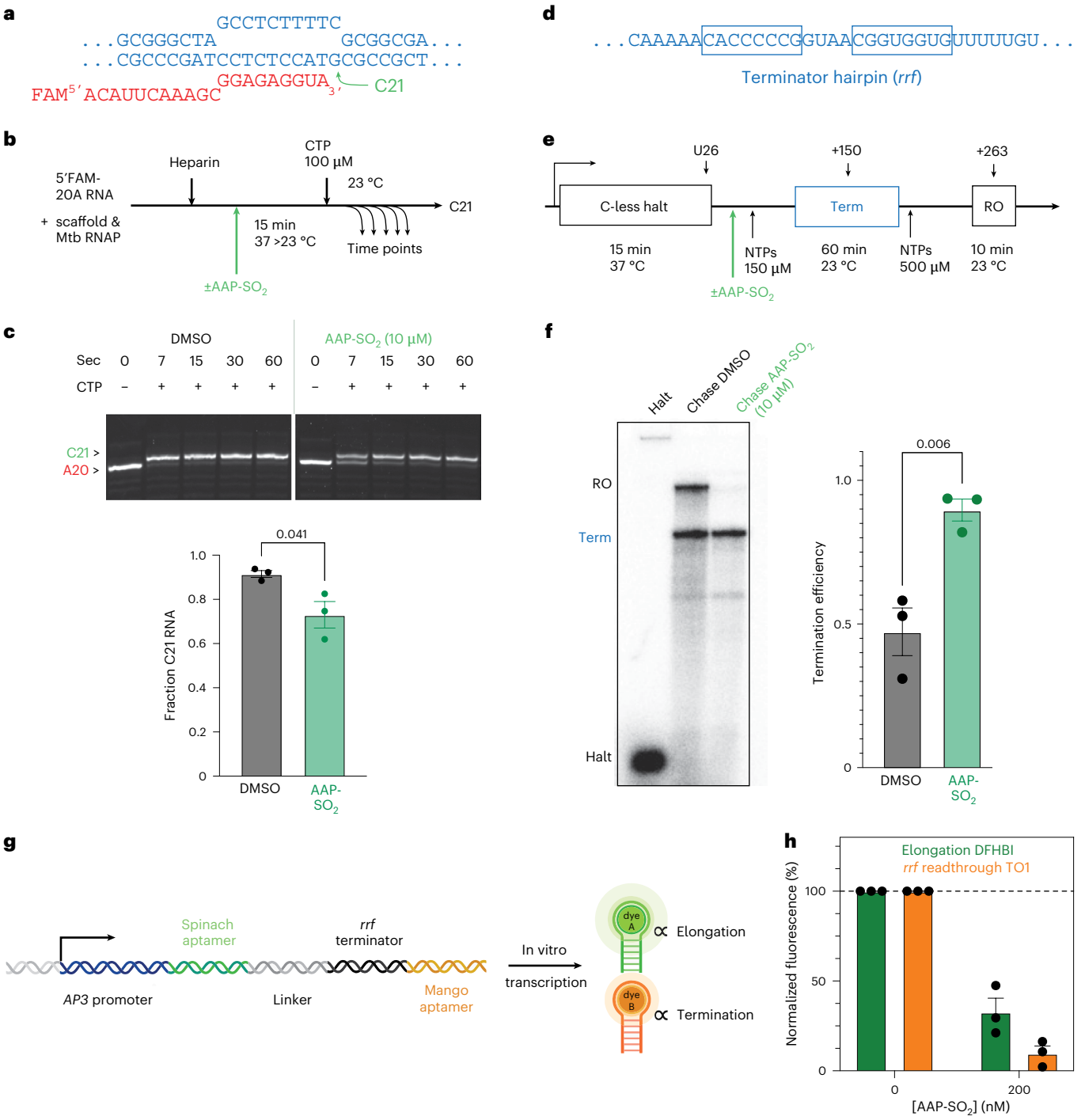

Fig. 2 | Effect of AAP-SO_2 on Mtb RNAP nucleotide addition and transcription termination. a, Sequence of the elongation scaffold used for nucleotide addition assays (see Methods for full sequences). The 3′ A represents position A20 of the RNA in the scaffold. The added CTP forms a 21-mer RNA (C21), representing a single NTP incorporation event. **b**, Schematic representation of the scaffold-based single-nucleotide addition assay to monitor the conversion of A20 to C21 using Mtb RNAP on a fluorescently (5′ 6-FAM fluorescein) labelled RNA in a DNA scaffold, as depicted in **a**. **c**, Fraction of C21 RNA formed at specific timepoints (0, 7, 15, 30 and 60 s) in the presence of DMSO (control) or AAP-SO_2. Bar graph represents the fraction of C21 RNA formed at 7 s as mean ± s.e.m. ($n = 3$ biological replicates, unpaired two-sided t-test, $p = 0.041$). **d**, Sequence of the *rrf* hairpin terminator used in the scaffold for the termination assay illustrated in **e**. **e**, Schematic representation of the in vitro termination assay using Mtb RNAP on a promoter-initiated template in the presence or absence of AAP-SO_2. The U26 C-less halt site is labelled ('Halt'), along with the termination site near +150 bases ('Term') and the run-off transcript at +263 bases ('RO'). **f**, Results of radioactive-based transcription assays to measure in vitro termination by Mtb RNAP on a promoter-initiated template in the presence or absence of AAP-SO_2 as schematized in **e** and as previously described[13]. Termination efficiency was calculated following the method of ref. 26. Data are presented as mean ± s.e.m. ($n = 3$ biological replicates, paired one-sided t-test, $p = 0.006$). **g**, Schematic of the aptamer-based transcription assay used to quantify elongation (spinach aptamer bound to DFHBI, green) and *rrf* readthrough (mango aptamer bound to TO1, orange). **h**, Percent fluorescence in the green (elongation) and orange (readthrough) channels in the presence of 200 nM AAP-SO_2 compared with the DMSO control (0) (mean ± s.e.m., $n = 3$ biological replicates).

https://doi.org/10.1038/s41564-025-02201-6

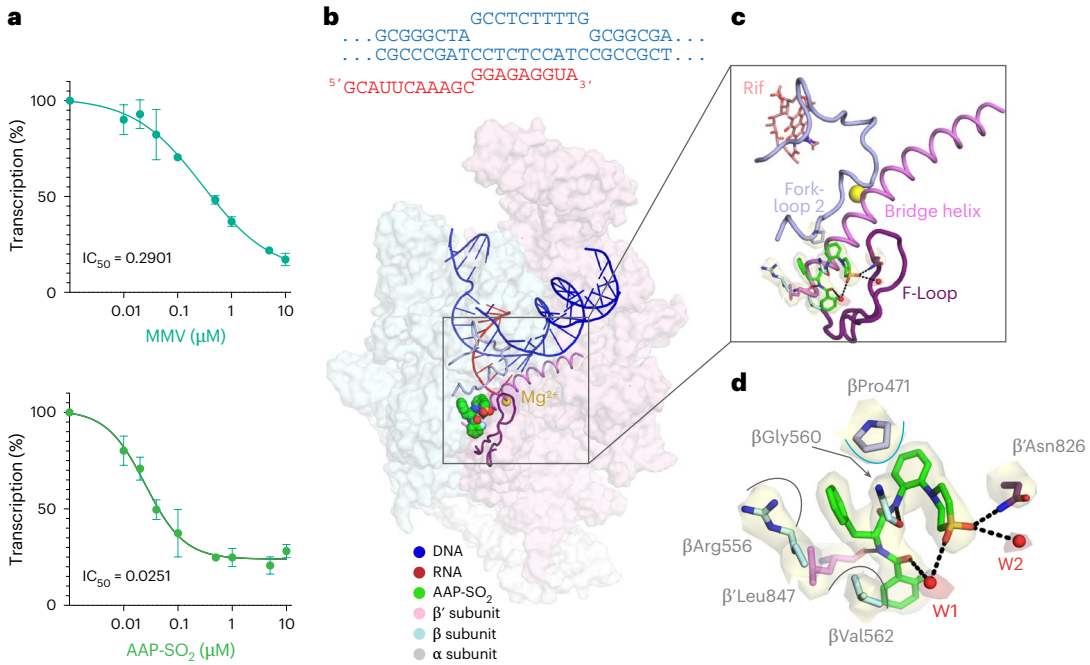

Fig. 3 | Structural basis of AAP-SO_2 binding and potency. a, IC_{50} determination of AAP-SO_2 and MMV688845 on Mtb RNAP transcription using a fluorescence-based aptamer assay. Data are presented as mean ± s.e.m ($n = 3$ biological replicates). **b**, Surface representation of the Mtb elongation complex structure, with AAP-SO_2 (shown as spheres). DNA is shown in cartoon as are protein features critical for AAP-SO_2 binding. **c**, Close-up view of the AAP-SO_2 binding site, highlighting interactions with RNAP features important for catalysis: Fork-loop 2, the Bridge-helix and the F-loop. Rif is modelled from structure 6CCV[100]. The polished, sharpened map is contoured at 7-σ around the protein and 5-σ around the modelled water molecules (W1 and W2). **d**, AAP-SO_2 forms six hydrogen bonds (black dashed lines) with RNAP and two water molecules (W1 and W2). These interactions include two hydrogen bonds between the protein and the sulfone group of AAP-SO_2, with one of them mediated by W1. In addition, AAP-SO_2 engages in π−CH interactions (light-blue arc) between βPro477 and AAP-SO_2 as well as hydrophobic interactions (grey arcs) with the Mtb core RNAP. Interactions were calculated using LIGPLOT[93] with a 3.5 Å cut-off for hydrogen bonds. The contouring in **c** matches those described in **b**. Validation statistics are listed in Extended Data Table 2.

by the compound. We therefore employed native mass spectrometry, which detects intact non-covalent complexes and the corresponding mass shift upon compound binding without requiring additional sample modification steps such as labelling, crosslinking or immobilization. Native mass spectrometry also serves as a reliable predictor of complexes suitable for downstream structural studies[40].

Using Rif as a positive control (Fig. 1b), we confirmed that the RNAP–Rif complex remains intact during native mass spectrometry analysis, validating the method's utility for identifying RNAP-binding small molecules. We then demonstrated with native mass spectrometry that both MMV688845 and AAP-SO_2 directly bind Mtb RNAP (Fig. 1c,d). Furthermore, AAP-SO_2 binds a higher fraction of the input RNAP than MMV688845 (Fig. 1c,d), consistent with the enhanced antimycobacterial activity of AAP-SO_2 (ref. 33).

AAP-SO_2 inhibits nucleotide addition

Chemically distinct CBR molecules, which inhibit *E. coli* but not Mtb RNAP, bind to a site predicted to overlap with the AAP-SO_2 binding site. This prediction is based on structural data of CBR-bound *E. coli* RNAP[38,39] and AAP-SO_2 resistance mutations observed in *Mycobacterium abcessus*[41]. CBR molecules have been shown to affect transcription elongation and pausing, probably by affecting nucleotide incorporation[37–39].

AAP-SO_2 is chemically related to MMV688845 and D-AAP1: all three compounds are diamides of D-phenylalanine, although they have distinct chemical modifications. AAP-SO_2 has a thiomorpholine dioxide structure (Fig. 1c,d) instead of a morpholine ring (MMV688845) or a methyl group (D-AAP1). In addition, in AAP-SO_2, the amino group of phenylalanine is amidated by 2-fluorobenzoic acid. D-AAP1 is known to inhibit Mtb transcription and kill Mtb[36]. However, the precise step of the transcription cycle that D-AAP1 affects remains unknown.

Having established that AAP-SO_2 directly binds to RNAP (Fig. 1d), we next examined its effect on Mtb transcription. Transcription elongation is a conserved multistep process that accomplishes phosphodiester bond formation in the RNAP active site, thereby adding nucleotides to the nascent RNA. The nucleotide addition cycle comprises four key events[24,42–45]: (1) Substrate NTPs load into the active site (the i + 1 site) and Watson–Crick base pair with the template DNA. (2) Catalysis occurs where a phosphodiester bond forms between the RNA 3′-O and the α-phosphate of the substrate NTP. (3) The substrate β- and γ-phosphates (in the form of pyrophosphate) are released as a by-product of bond formation. (4) Translocation of the RNA resets the active site to accept a new NTP in the i + 1 site.

To test AAP-SO_2's effect on a single NTP incorporation event (steps 1 and 2), we designed a nucleic acid scaffold that assembles with RNAP in the post-translocated state (Extended Data Table 1)[21,23], where the i + 1 NTP binding site is empty, and measured the extension of the RNA as a function of time in the presence or absence of AAP-SO_2 (Fig. 2a). In the absence of drug, the extension of the RNA transcript was already complete at the shortest timepoint measurable by manual pipetting (7 s). In the presence of AAP-SO_2, RNA extension was not complete until 30 s (Fig. 2c). Thus, AAP-SO_2 slows nucleotide addition (Extended Data Fig. 2a,b). These results provide insights into the mode of action of AAP-SO_2 in killing mycobacterial pathogens[41].

Since elongation and termination are kinetically competitive processes[26], we also examined AAP-SO_2's effect on termination. Strikingly, AAP-SO_2 increased the termination efficiency of Mtb RNAP from 45% to 85% at the Mtb *rrf* intrinsic terminator (Fig. 2d–f and Extended Data Fig. 2c). Although the overall transcription signal was reduced in the presence of AAP-SO_2, consistent with its function as an elongation inhibitor, we were nevertheless able to observe a shift in the ratio of termination to elongation. We next sought to confirm our

elongation and termination results using an independent approach. To do this, we adapted an aptamer-based in vitro transcription assay previously used to quantify initiation and elongation[46] by producing the spinach aptamer, incorporating the *rrf* terminator and adding a downstream mango aptamer to simultaneously measure readthrough efficiency (Fig. 2g). Consistent with the radioactive assay, we found that AAP-SO_2 reduces elongation rates to ~33% while increasing termination, as evidenced by a reduction of *rrf* terminator readthrough to 9.7% relative to no AAP-SO_2 (Fig. 2h). We further validated this assay using known pro-pausing factors NusA and NusG, which produced similar effects on elongation and termination (Extended Data Fig. 2f).

A key advantage of the aptamer assay compared to the radioactive assay is that RNAP bound by Rif can engage DNA as no RNA is pre-bound. Rif prevents assembly of elongation scaffolds because it clashes with the RNA[15]. We confirmed that Rif and Fdx inhibit spinach production, consistent with their known mechanisms (Extended Data Fig. 2d,e). These results highlight that AAP-SO_2 acts through a mechanism distinct from that of Rif and Fdx.

Structural basis of AAP-SO_2 binding and potency

We next compared the half-maximal inhibitory concentration (IC_{50}) values of MMV688845 and AAP-SO_2 using an aptamer-based in vitro transcription assay[46]. The increased in vitro potency of MMV688845 and AAP-SO_2 (IC_{50} of 0.290 vs 0.025 μM, respectively; Fig. 3a) reflects the higher in vivo potency (MIC_{90} of 0.494 μM vs 0.138 μM, respectively). We note that the calculated IC_{50} of AAP-SO_2 is below the enzyme concentration (0.1 μM) required for the assay. While this IC_{50} calculation serves as an estimation, it is clearly less than 0.05 μM, which represents the upper bound.

We then elucidated the structural basis for AAP-SO_2's increased potency against RNAP by solving the cryogenic electron microscopy (cryo-EM) structure of the Mtb RNAP core bound to AAP-SO_2 on an elongation scaffold (Fig. 3b and Extended Data Fig. 3a). The structure was resolved to a nominal resolution of 2.97 Å, with local resolution around the AAP-SO_2 molecule at 2.5 Å (Extended Data Table 2 and Extended Data Fig. 3b,c). Similar to D-AAP1 (ref. 36), AAP-SO_2 binds ~30 Å away from the RNAP active site Mg^{2+} and does not overlap with the Rif binding site (Fig. 3c). We note that the binding sites for CBR molecules and AAP-SO_2 are not conserved among bacterial clades or in eukaryotic RNAPs, RNAP I, RNAP II or RNAP III, explaining the lack of toxicity and off-target effects[37,41].

AAP-SO_2 interacts with three key features of RNAP involved in nucleotide addition: the β′ residues of the F-loop, the *N*-terminal part of the Bridge-helix and the β residues of Fork-loop 2 (refs. 47–51) (Fig. 3c,d). We predict that AAP-SO_2, similar to the CBR and D-AAP1 molecules, disrupts the positioning of the Bridge-helix, F-loop and Fork-loop 2, which are essential for nucleotide addition, thereby explaining the allosteric effects of AAP-SO_2 on elongation and termination.

AAP-SO_2 forms three hydrogen bonds with RNAP. Two of these contacts involve the amide group nitrogens of AAP-SO_2 acting as hydrogen bond donors to the carbonyl oxygens of RNAP βGly560 and β′Leu847 (located on the Bridge-helix). The observation of a hydrogen bond between the amide of AAP-SO_2 that interacts with βGly560 aligns with the observation that methylation of the amide group renders AAP-SO_2 ineffective[32]. The third hydrogen bond is formed between the sulfone oxygen (absent in D-AAP1) of AAP-SO_2 and the side-chain amide of β′Asn826 (part of the F-loop). This hydrogen bond explains AAP-SO_2's increased potency over other AAP molecules. Furthermore, we observed two additional interactions between the AAP-SO_2 sulfone group and two water molecules (Fig. 3d). AAP-SO_2's binding to Mtb RNAP is further strengthened by multiple hydrophobic interactions as well as a π–CH interaction between its benzene ring and βPro471 (Fig. 3c).

Finally, we compared our cryo-EM structure of the Mtb elongation complex with AAP-SO_2 to two crystal structures of RNAP inhibitors bound in similar binding pockets: CBR703 bound to *E. coli* RNAP (resolution 3.71 Å, PDB: 4XSX)[37] and D-AAP1 bound to Mtb RNAP (resolution 4.04 Å, PDB: 5UHE)[36].

The Mtb RNAP structure bound to AAP-SO_2 is similar to the Mtb RNAP/D-AAP1 structure, with a global root-mean-square deviation (RMSD) of 1.142 Å over 2,557 Cα atoms between the two structures (Extended Data Fig. 4a). However, notable local differences are observed in the rim helices and F-loop regions, which shift noticeably upon the binding of AAP-SO_2 versus D-AAP1 (Extended Data Fig. 4b). For the rim helices (β′737–794) and F-loop (β′816–840) alone, the RMSD was 2.69 Å over 82 Cα atoms, indicating substantial movement in these regions relative to the rest of the RNAP (Extended Data Fig. 4b). When the rim helices and F-loop were excluded from the RNAP alignment, the RMSD dropped to 1.128 Å over 2,517 atoms. This shift is explained by the interaction between the AAP-SO_2 sulfone (absent in D-AAP1) and β′N826. In addition, we note that some of the observed differences in the D-AAP1-bound RNAP structure could be influenced by crystal packing effects, known to cause local distortion in X-ray structures.

Lastly, sequence variations between the Mtb and *E. coli* binding pockets contribute to the differences in AAP-SO_2 binding to Mtb RNAP versus CBR binding to *E. coli* RNAP, particularly at residues βV568 and β′N826 (see alignment in Extended Data Fig. 4c). These structural and sequence-based differences, combined with the unique interactions of AAP-SO_2 offer valuable insights into the structure–activity relationships and will guide medicinal chemistry efforts towards developing future inhibitors targeting this pocket.

AAP-SO_2 reduces the frequency of Rif resistance

Mtb acquires Rif resistance through mutations in the Rif binding pocket that prevent Rif binding (Fig. 4a,b)[15]. The most frequent mutation in clinical Rif-resistant isolates occurs in the Rif resistance-defining region of the RNAP β-subunit: a single amino acid substitution of serine 450 to leucine (βS450L; Fig. 4a,b)[13,52].

While βS450L confers a fitness advantage in the presence of Rif, it results in a fitness defect in drug-free conditions (Extended Data Fig. 5a)[16,53,54]. This defect can be attributed, at least in part, to a slower elongation rate and higher termination efficiency in βS450L[13,14,55]. Consequently, βS450L is classified as a 'slow' RNAP

Fig. 4 | AAP-SO_2 shows increased activity against βS450L Mtb and slows the evolution of Rif resistance. a, Frequency of Rif-resistant *rpoB* mutations S450L, D435V and H445Y in clinical Mtb isolates (n = 14,729 Rif-resistant isolates)[13]. **b**, Structure of Rif bound to Mtb RNAP, highlighting the three most common Rif-resistance mutations[13,100]. **c**, Termination efficiencies of the βS450L RNAP in the absence (DMSO) or presence of AAP-SO_2. Data are presented as mean ± s.e.m. (n = 3 biological replicates, paired one-tailed t-test, p = 0.045). Absolute values are reported in Extended Data Table 3. **d**, MIC assay for AAP-SO_2 against otherwise isogenic WT H37Rv, βS450L and βH445Y mutant strains. Calculated MIC_{50} values for WT, βS450L and βH445Y are 67.0 ± 0.2, 43.4 ± 0.1 and 57.8 ± 0.1 nM, respectively. Data are mean ± s.e.m (n = 3 technical replicates). **e**,**f**, Time-kill experiment showing the effect of AAP-SO_2 on WT H37Rv and βS450L (**e**) and βH445Y (**f**) strains. Data points represent mean colony-forming units (c.f.u.) ml^{-1} at the indicated timepoints for duplicate biological cultures treated with AAP-SO_2 at 2.76 μM. LOR, limit of resolution; LOD, limit of detection. **g**, Schematic of the Rif-resistance fluctuation analysis. Twelve independent cultures were grown to $OD_{600} \approx 1–3$ in the presence of DMSO, 0.5× WT MIC_{90} AAP-SO_2 (=69 nM), or 0.5× WT MIC_{90} ethambutol (EMB) (=3.67 μM), then plated on RIF-free control plates or RIF 20× WT MIC_{90} (=243.0 nM) plates. **h**,**i**, Mutation rates (**h**) and mutational spectrum (**i**) from the modified Rif-resistance fluctuation analysis. Transparent dots represent mutation frequency (mutants per cell in a single culture; n = 12). Filled dots represent estimated mutation rates based on the Lea–Coulson model[101], with error bars showing the upper and lower limits. Statistical significance was determined by the maximum likelihood ratio value (p = 0.00001) using webSalvador[96]. Values are listed in Extended Data Table 4.

https://doi.org/10.1038/s41564-025-02201-6

mutant. In contrast, 'fast' RNAP mutants, such as βD435V and βH445Y, exhibit increased elongation rates and altered initiation rates[14], and together represent the second most common class of clinical Rif-resistant mutations (Fig. 4a,b). Notably, βH445Y mutant strains also show a fitness defect in the absence of Rif (Extended Data Fig. 5a)[16]. Importantly, both the βS450L and βH445Y Rif-resistant mutations do not alter the apparent binding affinity of AAP-SO_2 to the mutant RNAP (Extended Data Fig. 5b).

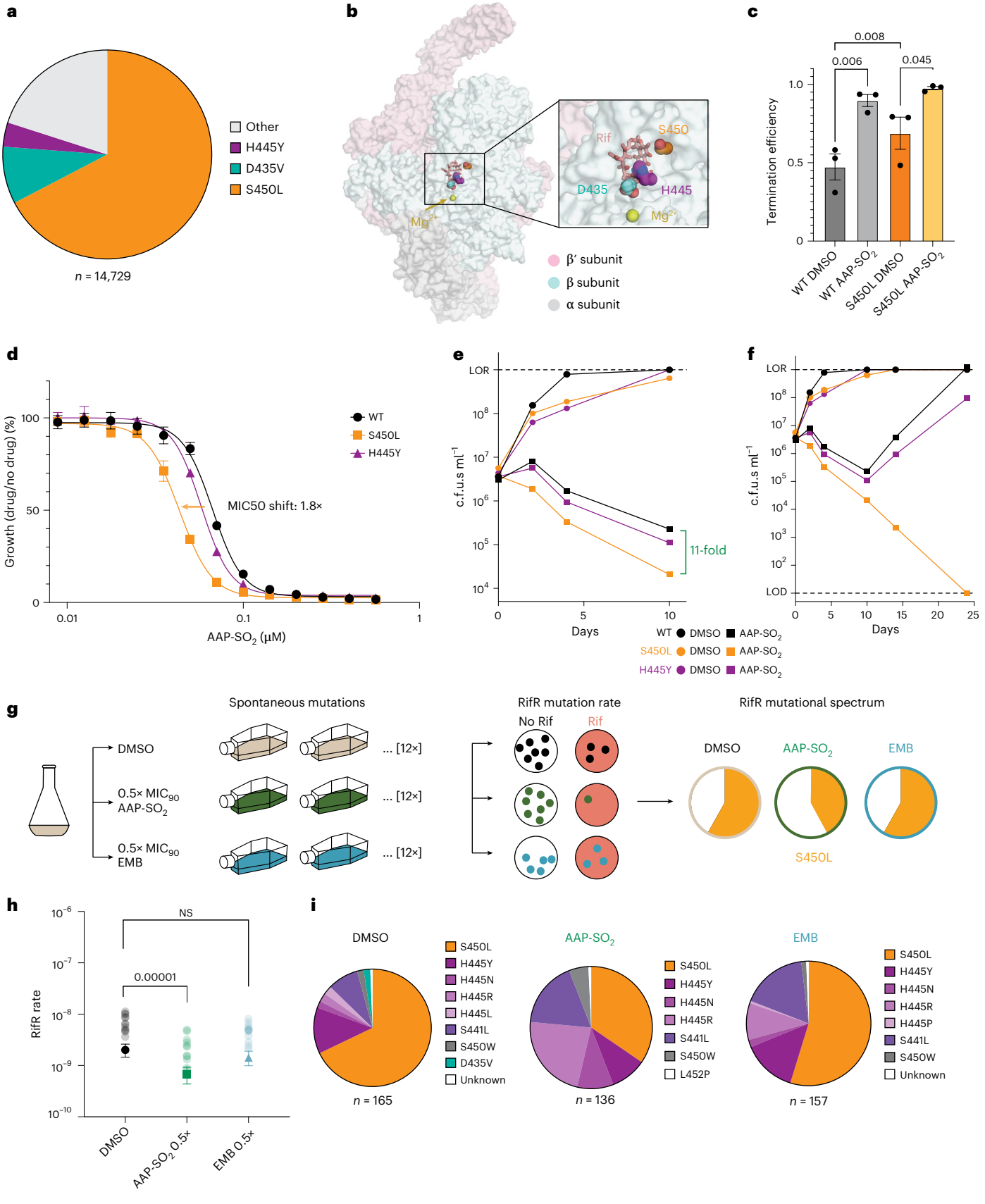

AAP-SO_2 slows nucleotide addition and increases termination efficiency (Fig. 2). We hypothesized that reducing elongation rates and increasing termination efficiency might exacerbate the functional vulnerability of βS450L RNAP and render it more sensitive to AAP-SO_2. To test this hypothesis, we performed termination assays on βS450L mutant RNAP on the *rrf* terminator, as described earlier (Fig. 2d–f). Relative to wild-type RNAP, βS450L mutant RNAP indeed has intrinsically higher termination efficiency, which is further exacerbated by AAP-SO_2 (Fig. 4c).

To assess whether the βS450L Mtb is more sensitive to AAP-SO_2, we next performed minimum inhibitory concentration (MIC) assays. βS450L displayed a small but reproducible ~2-fold MIC shift to AAP-SO_2 but not to EMB, a cell wall biosynthesis inhibitor[56] and negative control (Fig. 4d and Extended Data Fig. 5c). The effect of AAP-SO_2 on βS450L was more striking in time-kill experiments. We observed a ~11-fold increase in bactericidal activity of AAP-SO_2 against βS450L Mtb compared to WT RNAP over 10 days of drug exposure (Fig. 4e and Extended Data Fig. 5d). Even more striking, while WT and βH445Y Mtb strains developed resistance to AAP-SO_2, βS450L Mtb was sterilized under these experimental conditions (Fig. 4f and Extended Data Fig. 5e).

Reducing the rates of Rif resistance and biasing Mtb evolution away from fitter variants such as βS450L[16] could be therapeutically beneficial. Given the results from the time-kill assays, we hypothesized that AAP-SO_2's impact on elongation and termination might be unfavourable to the emergence of βS450L mutations. We therefore performed a modified Rif resistance fluctuation analysis[57] with dimethylsulfoxide (DMSO, vehicle control) or sub-MIC AAP-SO_2 or EMB (Fig. 4g). A low dose of AAP-SO_2 significantly reduced the overall Rif resistance mutation rate compared to DMSO and EMB (Fig. 4h). Consistent with our prediction, sequencing of the Rif resistance-determining region (Extended Data Table 1) revealed that exposure to AAP-SO_2 altered the mutational spectrum: 34.6% of Rif-resistant colonies from the AAP-SO_2 condition harboured βS450L mutations, compared with 67.9% in the DMSO and 54.8% in the EMB conditions (Fig. 4i). These results suggest that targeting of functional vulnerabilities in transcription can reduce and alter the evolutionary spectrum of Rif resistance.

Vertical inhibition of transcription enhances killing of non-replicating Mtb

Having established the effect of AAP-SO_2 monotherapy on βS450L Mtb and its impact on the evolution of Rif resistance, we next investigated the potential of AAP-SO_2 in combination therapy with Rif. We hypothesized that combining two RNAP inhibitors that target the same pathway but operate with different mechanisms could synergistically enhance efficacy against TB.

We first tested the activity of Rif and AAP-SO_2 in combination against actively replicating Mtb. The results showed additive effects of the two compounds (Fig. 5a). Next, we examined the effect of combining Rif and AAP-SO_2 to kill non-replicating bacteria present in caseum derived from granulomas from Mtb-infected rabbits. The rabbit caseum model is an established ex vivo system for investigating the bactericidal activity of antitubercular compounds against non-replicating Mtb in necrotic granulomas[8,58,59] (Fig. 5b).

Using this model, we found that AAP-SO_2 killed non-replicating Mtb at a caseum minimal bactericidal concentration (casMBC$_{90}$) of 7.89 μM, lower than Rif's casMBC$_{90}$ of 16.6 μM (Fig. 5c). Next, Rif and AAP-SO_2 were tested in combination at equimolar concentrations. The combination of 0.5 μM of each compound was sufficient to kill over 90% of the Mtb inoculum in 7 days (casMBC$_{90}$ = 0.49 μM), outperforming the bactericidal potency of the individual compounds. Further investigation of the dose–response data revealed that Rif and AAP-SO_2 are highly synergistic[60,61] at equimolar concentrations of 0.5 μM and 2 μM in this ex vivo model (Fig. 5d).

Lastly, we tested additional combinations of RNAP inhibitors targeting specific steps of the Mtb transcription cycle. We combined the clinically available drug Fdx with Rif. In rich media, Fdx potentiated Rif killing, similar to AAP-SO_2 (Extended Data Fig. 6a). However, in the granuloma synergy assay, Fdx showed no activity, either alone or in combination, confirming that it is not a strong candidate for TB treatment (Extended Data Fig. 6b). One explanation for the low bactericidal activity of Fdx in granulomas is the poor stability at the infection site (Extended Data Fig. 6c), although other possibilities remain. By contrast, it is encouraging that AAP-SO_2 is stable and active in the granuloma model. These findings support the rationale for evaluating future, more stable Fdx derivatives in combination with Rif, as well as additional RNAP inhibitors acting at distinct transcriptional stages in granuloma synergy assays.

Discussion

The substantial global disease burden of drug-sensitive and drug-resistant Mtb infections necessitates the development of new treatments. Rif-resistant mutations reduce the cure rate by ~50% (ref. 11). Yet, these same Rif-resistant mutations impose a fitness cost on bacteria in the absence of Rif[13,14,16]. This fitness cost creates an opportunity for rational therapeutic approaches that exploit these vulnerabilities to limit the emergence and spread of drug-resistant TB[62,63]. Here we show that this rationale can successfully be applied to one of Mtb's most essential biological pathways—transcription.

Previous studies showed that slow RNAP mutants, such as βS450L Rif-resistant Mtb, reduce elongation rates and lead to hypertermination[13,14], revealing a 'functional vulnerability' of RNAP and explaining the fitness cost of this mutation. We therefore developed a pipeline to identify inhibitors targeting this functional vulnerability in the transcription cycle for both WT and Rif-resistant RNAPs. We define functional vulnerabilities as enzyme or pathway dependencies arising from resistance-conferring mutations, which render the strain hypersensitive to specific drugs or combinations targeting distinct functional steps. Functional vulnerabilities are an extension of collateral sensitivities—an evolutionary trade-off where resistance to one antibiotic increases sensitivity to another[64,65], leveraging mechanistic insights into the fitness costs imposed by resistance mutations to identify more efficacious inhibitors. Our approach highlights the potential for leveraging a mechanistic understanding of transcription to identify targetable vulnerabilities and guide the development of combination therapies against drug-resistant pathogens.

We demonstrated that AAP-SO_2 inhibits nucleotide addition, thereby reducing elongation and increasing termination rates. In line with termination being a functional vulnerability in βS450L Rif-resistant Mtb, AAP-SO_2 shows elevated bactericidal activity against this strain. Termination is less functionally vulnerable in WT and the fast RNAP βH445Y Rif-resistant mutant and the bactericidal effect of AAP-SO_2 on these strains was less. In addition, AAP-SO_2 reduced the frequency of Rif resistance and skewed the mutational spectrum, reducing yet not eliminating the occurrence of βS450L mutations.

Drawing parallels with precision medicine in cancer therapy, where genetic insights inform combination strategies, our findings put forward the possibility of precision targeting for Mtb: selecting antibiotic combinations—here a compound targeting promoter escape such as Rif with one targeting termination such as AAP-SO_2—on the basis of pathogen-specific genetic and functional alterations—in this case, hypertermination in βS450L Rif-resistant strains. Molecular diagnostic approaches such as GeneXpert already enable rapid identification of Rif-resistant mutations[66,67]. It would therefore be possible to use such information for a precision targeting approach and make a rational selection of combination therapies tailored to individual patients, maximizing efficacy and minimizing the development of drug resistance.

Given the effects of AAP-SO_2 on the evolution of Rif resistance, we next studied Rif and AAP-SO_2 in combination. The transcription cycle itself operates as a sequential biological pathway, where each step is connected and dependent on the previous one. By targeting

https://doi.org/10.1038/s41564-025-02201-6

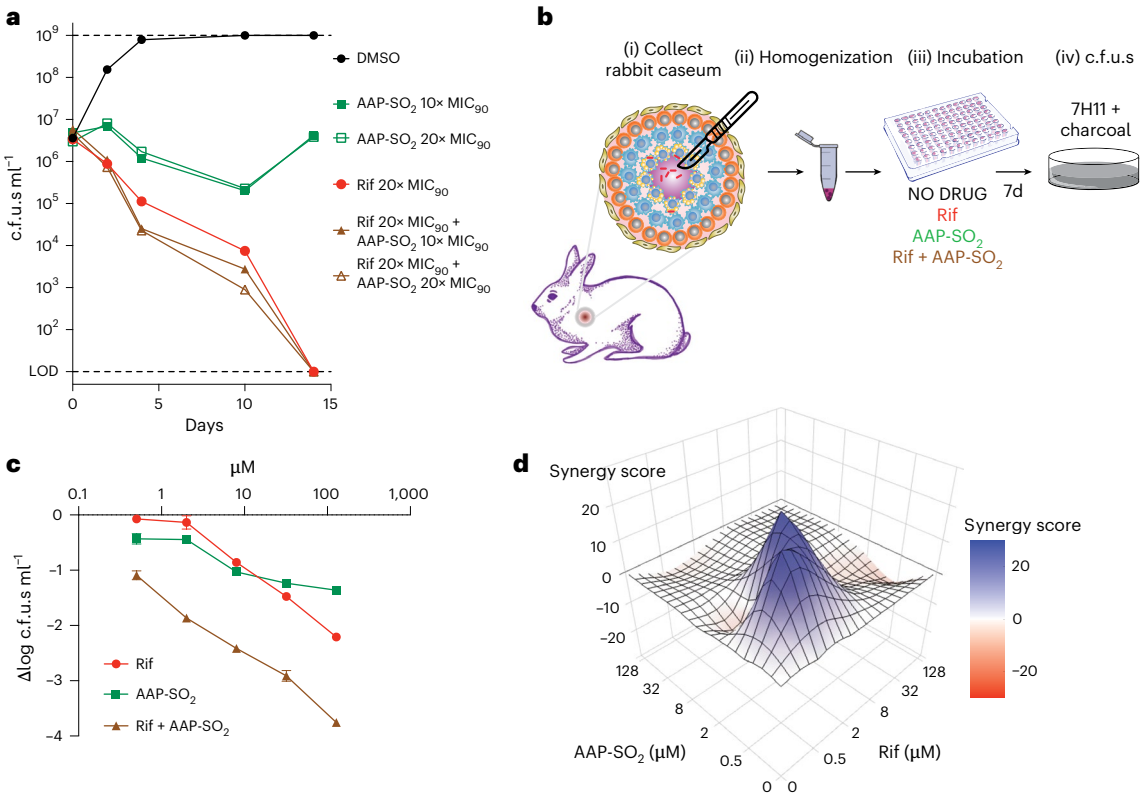

Fig. 5 | Vertical inhibition of transcription by Rif and AAP-SO_2 kills replicating and non-replicating Mtb. a, Time-kill experiment showing the effect of DMSO (control), AAP-SO_2 monotherapy (10× WT MIC_{90} = 1.38 μM and 20× WT MIC_{90} = 2.76 μM), Rif monotherapy (20× WT MIC_{90} = 243 nM), and the combination of Rif (20× WT MIC_{90} = 243 nM) and AAP-SO_2 (10× WT MIC_{90} = 1.38 μM and 20× WT MIC_{90} = 2.76 μM) on WT Mtb c.f.u. ml^{-1} over the course of 10 days. Data represent the mean from duplicate biological replicates. **b**, Schematic of the ex vivo rabbit caseum experiment. Caseum from granulomas of rabbits infected with HN878 Mtb was excised (i), homogenized (ii), divided into 96-well plates and exposed to equimolar amounts of Rif and AAP-SO_2 for 7 days (iii). Bacterial killing was assessed by plating on 7H11 agar with charcoal and counting c.f.u. (iv). **c**, Bactericidal activity of AAP-SO_2, Rif, and the combination of Rif and AAP-SO_2 in the ex vivo rabbit caseum model. The log(fold change) in c.f.u. ml^{-1} relative to the vehicle-only control is reported. Each data point represents mean ± s.d. from 3 experimental replicates. **d**, Synergy calculation using the Bliss independence model for Rif and AAP-SO_2 in the ex vivo caseum model. The synergy scores for Rif and AAP-SO_2 at 0.5 μM and 2 μM each are 23.4 ± 4.9 and 24.9 ± 2.9, respectively. The scores represent mean ± s.d. (n = 3) and were plotted using Synergyfinder[102].

multiple steps within this pathway—referred to as 'vertical inhibition'—we hypothesized that it is possible to disrupt the overall functionality of the transcription process more effectively than targeting a single step. Vertical inhibition exploits the interdependence of pathway steps to enhance therapeutic outcomes and may also enhance treatment efficacy by achieving comprehensive pathway suppression while preventing compensatory feedback loops that often drive drug resistance[68]. This strategy has proven highly effective in cancer therapies targeting pathways such as RAS and mTOR[69–71], and its potential in antibiotic therapy is highlighted by the synergy of trimethoprim and sulfamethoxazole, two inhibitors of the folate biosynthesis pathway[72,73], and Synercid, a clinically approved dual antibiotic that targets distinct steps in protein synthesis[74]. Similarly, we propose that vertical inhibition of the transcription cycle in Mtb can be leveraged to overcome resistance and enhance therapeutic outcomes.

We show that Rif and AAP-SO_2 have additive effects on replicating bacteria. Importantly, our findings also highlight the therapeutic potential of vertical inhibition in addressing extreme drug tolerance, as seen in slow-growing and non-replicating Mtb within granulomas and caseum. Vertical inhibition of transcription with Rif and AAP-SO_2 enhances the efficacy of both compounds against non-replicating Mtb. Novel regimens that effectively reach and kill non-replicating persistent bacteria in caseous lesions may improve cure rates and shorten treatment duration[75].

Despite its promise, AAP-SO_2 remains a tool compound with low microsomal stability. Yet, ongoing medicinal chemistry efforts, such as structure-guided optimization and scaffold hopping to more drug-like derivatives, have already shown promise to enhance its bioavailability[32]. Other approaches to improve the pharmacokinetic properties of AAPs could include increasing bioavailability through targeted cytochrome P450 (CYP) inhibition or exploring pulmonary administration as a strategy to bypass hepatic metabolism.

Our findings endorse the development of combination therapy with rifamycins and AAPs against mycobacteria, in addition to the potential for using AAPs as components of TB drug regimens with entirely new modes of action. In parallel, our work sets the stage for the identification of other druggable functional vulnerabilities in transcription and other multistep biological cycles. For example, it is likely that fast Rif-resistant mutants harbour distinct transcriptional dependencies that can be rationally targeted. We note that the synergy of AAP-SO_2 with Rif is specific to non-replicating bacteria in granuloma models, indicating that transcription is a key targetable pathway in this cell state and environment. Lastly, our work highlights the need for expanded genetic studies to better understand the physiology of non-replicating bacteria in caseum, with the goal of identifying additional environment-specific, druggable pathways.

In conclusion, our work underscores the importance of understanding functional vulnerabilities within essential pathways such as transcription for advancing combination therapy. By exploiting the

balance between elongation and termination in βS450L Rif-resistant Mtb, we achieved increased killing compared with wild-type and βH445Y mutant Mtb. Furthermore, AAP-SO_2 demonstrated bactericidal activity in rabbit caseum and synergized with Rif in this environment. These findings support the potential of vertical inhibition of transcription to improve TB treatment outcomes, particularly in challenging contexts such as non-replicating bacteria. Precision targeting, which involves integrating biochemical insights with genetic data, offers a roadmap for innovative therapeutic strategies that optimize treatment success and limit resistance development.

Methods

Ethics approval

Animal studies were conducted with appropriate ethics guidelines and regulations. The studies were carried out with approval from the Institutional Animal Care and Use Committees of the National Institute of Allergy and Infectious Diseases, NIH (protocol number LCIM-3). Female New Zealand White rabbits (Millbrook Farm, Concord, MA) were maintained under specific pathogen-free conditions and fed water and chow ad libitum. Rabbits were infected with *Mycobacterium tuberculosis* HN878 using a nose-only aerosol exposure system. The infection was allowed to progress for 12–16 weeks before necropsy. The right and left lungs were removed and weighed. For this study, caseum was collected from rabbits engaged in other experiments.

Bacterial cultures

E. coli strains are derivatives of DH5α (NEB), Rosetta2 or BL21(DE3) (Novagen). Mtb strains are derivatives of H37Rv, Harvard strain. *E. coli* strains were grown in LB broth or on LB agar supplemented with the appropriate antibiotics (50 μg ml^{-1} kanamycin and/or 34 μg ml^{-1} chloramphenicol). Mtb was grown at 37 °C in Difco Middlebrook 7H9 broth or on 7H10 agar supplemented with 0.2% glycerol (7H9) or 0.5% glycerol (7H10), 0.05% Tween-80 and 1× oleic acid-albumin-dextrose-catalase (OADC). Mtb cultures were maintained under static growth conditions in tissue culture flasks (fluctuation assay) or 384-well plates (MIC assays) with 5% CO_2.

Antibiotics

For the synthesis and analytical characterization of AAP-SO_2, we refer to substance no. 24 in ref. 31. Rifampicin, ethambutol dihydrochloride and fidaxomicin were sourced commercially from Gold Biotechnology (R-120-10), Sigma-Aldrich (E4630-25G) and Thermo Fisher (AC468312500), respectively.

Protein purification

Mtb RNAP. Wildtype Mtb RNAP was purified as previously described[27]. Briefly, WT *Mtb* RNAP was overexpressed in *E. coli* Rosetta2 cells using plasmid pMP61, a kanamycin-resistant plasmid that contains a T7 promoter, followed by *rpoA*, *rpoZ*, a linked *rpoBC* and a His_8-tag. The *rpoB–rpoC* fusion minimizes the possibility of *E. coli* β or β′ intermixing with *Mtb* subunits. A single pMP61 transformed Rosetta2 colony was then expanded in LB broth with 50 μg kanamycin ml^{-1} and 34 μg chloramphenicol ml^{-1} at 37 °C to an optical density at 600 nm (OD_{600}) of ~0.3. The temperature was then lowered to 25 °C and the culture was left shaking to an OD_{600} of ~0.6. Then, RNAP expression was induced by adding 0.1 mM isopropyl β-D-1-thiogalactopyranoside (IPTG; Gold Biotechnology, 1248), grown overnight for 16 h and collected by centrifugation (4,000 *g*, 20 min, 4 °C). Collected cells were resuspended in lysis buffer (50 mM Tris-HCl, 5% glycerol pH 8.0, 1 mM EDTA, 5 mM dithiothreitol (DTT), 1 mM phenylmethyl sulfonyl fluoride and 1 mM protease inhibitor cocktail) and lysed by 3 passages on a French Press (Avestin). The lysate was centrifuged twice (27,000 × *g*, 15 min, 4 °C). Next, Polymin P (PEI, Thermo Fisher, AC178572500) was added to the supernatant to a final concentration of 0.6% (w/v) and the mixture was left stirring for 15 min to precipitate DNA binding proteins including RNAP before being pelleted using centrifugation (11,000 × *g*, 15 min, 4 °C). The pellet was then washed three times in TGED wash buffer (10 mM Tris-HCl pH 8.02, 5% v/v glycerol, 0.1 mM EDTA, 5 mM DTT, 300 mM NaCl) to remove non-target proteins. Upon centrifugation (11,000 × *g*, 15 min, 4 °C), RNAP was eluted from the pellet using elution buffer (10 mM Tris-HCl pH 8.02, 5% v/v glycerol, 0.1 mM EDTA, 5 mM DTT, 1 M NaCl). Next, RNAP was precipitated overnight at 4 °C using 3.5 g l^{-1} pulverized $(NH_4)_2SO_4$. Upon centrifugation (11,000 × *g*, 40 min, 4 °C), the precipitate was dissolved in Nickel buffer A (20 mM Tris pH 8.0, 5% glycerol, 1 M NaCl, 5 mM β-mercaptoethanol, 10 mM imidazole) and loaded onto two HisTrap FF 5 ml columns (GE Healthcare Life Sciences) washed with Nickel buffer A. RNAP was eluted from the column with Nickel buffer B (20 mM Tris pH 8.0, 5% glycerol, 1 M NaCl, 5 mM β-mercaptoethanol, 250 mM imidazole). Lastly, eluted RNAP was run over a gel filtration column (HiLoad Superdex 26/600 200 pg) in gel filtration buffer (10 mM Tris pH 8.0, 5% glycerol, 0.1 mM EDTA, 500 mM NaCl, 5 mM DTT). Eluted samples were flash frozen in liquid nitrogen and stored at −80 °C until usage. βS450L and βH445Y Mtb RNAP were produced using mutated pMP61 plasmids (generous gift of the Landick lab) and purified as described above.

Mtb σ^A–RbpA. Mtb σ^A–RbpA was purified as previously reported[76]. Briefly, His12-tagged Mtb σ^A and untagged Mtb RbpA were overexpressed in *E. coli* BL21(DE3) cells (Novagen) using a pCDFDuet-1 vector (Novagen) and pET-21C vector (Novagen), respectively. Protein production was induced with 0.5 mM IPTG overnight at 18 °C, followed by protein purification using Ni^{2+}-affinity chromatography. Following elution, the complex was dialysed, and the His-tag was cleaved with precision protease. The cleaved complex was further purified by a second Ni^{2+}-affinity column, followed by size exclusion chromatography (SuperDex-200 16/16, GE Healthcare Life Sciences). Eluted samples were flash frozen in liquid nitrogen and stored at −80 °C until usage.

Mtb CarD. Mtb CarD was overexpressed as previously described[77,78]. Briefly, Mtb CarD was overexpressed in BL21(DE3) (Novagen) cells using a pET SUMO vector (Invitrogen). Expression was induced with 1 mM IPTG for 4 h at 28 °C. The overexpressed-protein purification was performed using Ni^{2+}-affinity chromatography. The eluted protein was then cleaved with the SUMO protease ULP1 (Invitrogen, 12588018) and loaded onto a Ni^{2+}-affinity column. The flow-through was further purified by size exclusion chromatography (Superdex 200, Cytiva), aliquoted and snap frozen for storage and further use.

Native mass spectrometry analysis

Frozen wild-type, βS450L and βH445Y Mtb RNAP core samples were thawed and buffer exchanged twice into 500 mM ammonium acetate pH 7.5 and 0.01% Tween-20 using Zeba microspin desalting columns with a 7-kDa molecular weight cut-off (Thermo Fisher). The sample concentration was then measured using the Nanodrop spectrophotometer. For small-molecule binding experiments, the RNAP core complex (typically at 1.5–1.6 μM) was mixed with 10 μM compound (~6-fold molar excess) and incubated at 37 °C for 10 min. The stock solutions for the compounds were in DMSO and the final DMSO concentration after dilution and mixing with RNAP core before native mass spectrometry analysis was 0.2–0.7% v/v.

For native mass spectrometry characterization, a 2–3-μl aliquot of the sample was loaded into a gold-coated quartz capillary tip that was prepared in-house and then electrosprayed into an Exactive Plus with extended mass range (EMR) instrument (Thermo Fisher) with a static direct infusion nanospray source[79]. The typical native mass spectrometry parameters included: spray voltage, 1.20–1.22 kV; capillary temperature, 150 °C; in-source dissociation, 10 V; S-lens RF level, 200; resolving power, 8,750 or 17,500 at m/z of 200; AGC target, 1×10^6; maximum injection time, 200 ms; number of microscans, 5; total number of scans, at least 100. Additional native mass spectrometry parameters

were: injection flatapole, 8 V; interflatapole, 4 V; bent flatapole, 4 V; high energy collision dissociation (HCD), 200 V; ultrahigh vacuum pressure, 3.4–6.0 × 10^{-10} mbar. Mass calibration in positive extended mass range mode was performed using caesium iodide. For data processing, the collected native mass spectrometry spectra were visualized using Thermo Xcalibur Qual Browser (v.4.2.47). Spectral deconvolution was performed using UniDec (v.4.2.0)[80,81] with the following general parameters: smooth charge state distribution, enabled; peak shape function, Gaussian; degree of softmax distribution (beta parameter), 10.

The expected masses for the component proteins of the Mtb RNAP core complex include: α, 37,706.4 Da; fused β and β′, 277,907.0 Da (N-terminal methionine removed, includes two Zn^{2+} ions with each ion coordinated to four cysteines and one Mg^{2+} ion); and ω, 11,768.1 Da (N-terminal methionine removed). The observed mass deviations (calculated as the % difference between the measured and expected masses relative to the expected mass) ranged from 0.006–0.03%.

Scaffold-based nucleotide addition assay

20-mer 5′ FAM-labelled elongation complex RNA and template DNA (T-DNA) and non-template DNA (NT-DNA) were synthesized by Integrated DNA Technologies (IDT) (Extended Data Table 1). T-DNA (33.25 μM) and the labelled RNA (25 μM) were then annealed in annealing buffer (20 mM Tris, 25 mM K-glutamate, 10 mM MgOAc, 1 mM DTT, 5 μg ml^{-1} BSA) using a thermocycler (95 °C for 2 min, 75 °C for 2 min, 45 °C for 5 min and from 43–23 °C for 2 min per 1 °C decrease). Elongation complexes (EC) were reconstituted by incubating 125 nM EC RNA, 165 nM T-DNA and 1 μM Mtb core RNAP (final concentration) in elongation buffer for 5 min at 37 °C. NT-DNA (500 nM) was added, and the mixture was incubated for an additional 5 min at 37 °C. Heparin (50 μg ml^{-1}) was added to prevent the formation of non-specific interactions. After incubation with DMSO (10% v/v) or 10 μM AAP-SO_2 at 37 °C for 5 min and bringing the mixture to 23 °C over 10 min, the elongation complex RNA was extended by addition of cytidine triphosphate (CTP) (100 μM final concentration). At set timepoints (0, 7, 15, 30 and 60 s), aliquots (5 μl) were removed and combined with 5 μl 2× stop buffer (95% formamide, 20 mM EDTA, 0.05% bromophenol blue, 0.05% xylene cyanol). Samples were then run on a 23% denaturing PAGE gel for 1.5 h at 1,060 kV and imaged using a ChemiDoc MP system (BioRad).

Quantification of the nucleotide addition assay was done using ImageJ software (NIH) and Igor Pro 9.5 (WaveMetrics). Each lane of the gel image was first converted to a pseudo-densitometer plot using the ImageJ rectangle and plot profile function. The resulting values were then imported as a text file into Igor Pro and the peak areas for A20 (20-mer RNA) and C21 (21-mer RNA; 1 nucleotide addition) were measured using Multipeak fit v.3.00 (setting: Gauss).

Fraction C21 was calculated as:

$$\frac{\text{C21 peak area}}{\text{A20 + C21 peak areas}}$$

Statistical differences in the C21 fraction due to the exposure to AAP-SO_2 were calculated in GraphPad Prism v.10.4.1 using a two-sided, unpaired *t*-test with no assumptions on variance.

Promoter-based termination assay

The promoter-based termination assay was performed as previously described[82] but with a few modifications. In brief, plasmid pJC1 was used to PCR amplify linear DNA containing a C-less halt cassette (+1 to +26), an Mtb intrinsic terminator sequence (*rrf* gene) approximately +150 bp and a run-off at approximately +263 bp. WT or S450L holo-RNAP (200 nM) was incubated for 15 min at 37 °C with 500 nM CarD and template DNA (10 nM) in transcription buffer (20 mM Tris, 25 mM K-glutamate, 10 mM MgOAc, 1 mM DTT, 5 μg ml^{-1} BSA) at 37 °C. Transcription was initiated by adding ATP + GTP (both at 16 μM final concentration), UTP (2 μM) and 1.25 μCi (15 nM) per reaction [α-^{32}P] UTP (Perkin Elmer, BLU007H250UCI) for 15 min at 37 °C (Halt). The complex was then exposed to DMSO (10% v/v) or AAP-SO_2 (10 μM final concentration) for 10 min at 37 °C and brought to 23 °C. Transcription was restarted by adding a master mix containing NTP mix (A + C + G + U, all at 150 μM final concentration) and heparin (10 μg ml^{-1}). The reaction was allowed to proceed for 60 min, followed by a 'chase' reaction in which all 4 nucleotides were added (each at 500 μM final concentration). After 10 min, the reaction was stopped and added to a 2× stop buffer (95% formamide, 20 mM EDTA, 0.05% bromophenol blue, 0.05% xylene cyanol). Samples were analysed on an 8% denaturing PAGE (19:1 acrylamide:bis acrylamide, 7 M urea, 1× TBE pH 8.3) for 1.25 h at 400 V, and the gel was exposed on a storage phosphor screen and imaged using a Typhoon PhosphoImager (GE Healthcare).

Quantification of termination. Quantification of termination efficiency was performed as previously described[13]. In ImageJ software (NIH), each lane of the gel image was converted to a pseudo-densitometer plot using the ImageJ line function, and the relative areas of the termination (+150 bp) and run-off bands (+263 bp) were measured. Absolute values can be found in Extended Data Table 3.

Termination efficiency was calculated as:

$$\frac{\text{termination (term) peak area}}{\text{total of the termination and run − off (term + run − off) peak areas}}$$

Statistical differences in termination efficiency due to the βS450L mutation and/or the exposure to AAP-SO_2 were calculated in Prism using a one-sided, paired *t*-test with no assumptions on variance

Aptamer-based elongation and readthrough assay

Elongation and readthrough were measured using a modified version of a previously described fluorescent-aptamer-based transcription assay[46]. First, a DNA gBlock containing the AP3 promoter, the spinach mini-RNA sequence, an Mtb terminator (*rrf*) and the MangoIV RNA sequence (Extended Data Table 1) was synthesized by IDT, amplified with M13 forward and reverse primers, and PCR purified. Then, 50 nM of Mtb WT RNAP holoenzyme and CarD (1 μM) were mixed in transcription buffer (20 mM Tris-HCl pH 7.9, 50 mM KGlu, 10 mM $MgCl_2$, 1 mM DTT and 5 μg ml^{-1} bovine serum albumin). Next, DMSO (control, 15% v/v), Rif (200 nM), Fdx (2,000 nM), AAP-SO_2 (200 nM) or NusA/G (1 μM each) were respectively added to the mix and incubated at 37 °C for 5 min. Then, the amplified DNA (10 nM) was added to each tube, and the samples were incubated for an extra 15 min at 37 °C to allow RNAP open complex formation. Then, RNAse inhibitor (0.4 U $μl^{-1}$; Thermo Fisher, EO0381), 3,5-difluoro-4-hydroxy benzylidene imidazolinone (DFHBI; Sigma-Aldrich, SML1627; 20 μM), a GFP fluorophore mimic activated by binding to the spinach aptamer and Thiazole Orange-1 (TO1-3PEG-Biotin; Applied Biological Material, G7955) were added to the mix and the reactions transferred to a flat black 384-well plate (Greiner, 781209). Transcription was initiated by adding NTPs (500 μM ATP + CTP + GTP + UTP) to each well. Next, each reaction was imaged every 30 s for a total of 30 min inside a Tecan Spark plate reader kept at 37 °C. The DFHBI fluorescence signal was read at 440 ± 15 nm excitation, 490 ± 15 nm emission and 150 gain. The TO1 fluorescence was read at 520 ± 15 nm excitation, 555 ± 15 nm emission and 150 gain. The measured fluorescence was then plotted in GraphPad Prism and analysed using the 'simple linear regression' function. Slopes from three independent data sets where then normalized to the slopes of the no drug (DMSO) or no factor (no NusA/G) controls, and the decrease in elongation and *rrf* readthrough rates was calculated.

Cryo-EM of Mtb RNAP elongation complex bound to inhibitor AAP-SO_2

Preparation of elongation complexes for cryo-EM. The DNA oligonucleotides for the elongation complex scaffolds were obtained

from IDT and RNA oligonucleotides were obtained from GE Healthcare Dharmacon. To prepare the sample, T-DNA and RNA were first annealed in annealing buffer (10 mM HEPES pH 7.5, 1 mM EDTA, 50 mM NaCl) in a 1:3 ratio for 5 min at 95 °C, brought to 23 °C and then stored on ice until use. Next, Mtb core RNAP was dialysed overnight into cryo-EM buffer (20 mM HEPES pH 7.5, 150 mM KGlu, 5 mM MgOAc, 2.5 mM DTT), combined with the T-DNA:RNA hybrid (1:1.3 molar excess) and incubated at 23 °C for 15 min. Then, NT-DNA was added to the complexes at 1.5:1 molar excess with the T-DNA:RNA and incubated at 23 °C for 10 min, followed by size exclusion chromatography (Superose 6 Increase 10/300 GL column, Cytiva). Upon concentration of the complex (15.5 µM), AAP-SO_2 at 25:1 molar excess was added and the mixture incubated at 37 °C for 15 min before applying it to the grids.

Cryo-EM grid preparation. Glow-discharged C-flat holey carbon grids (CF-1.2/1.3-4Au, Photochips) were used for cryo-EM imaging. Of the sample (see above), 3.5 µl was mixed with *n*-octyl-*β*-D-glucoside (OG; final concentration 0.1% (w/v); Anatrace, O311) and applied to the grid. Using a Vitrobot Mark IV (Thermo Fisher), grids were then blotted and plunge frozen into liquid ethane with 100% chamber humidity at 22 °C.

Cryo-EM data acquisition and processing. Grids were imaged using a 300 keV Titan Krios cryo-electron microscope (Thermo Fisher) equipped with a K3 Gatan direct electron detector. Cryo-EM data collection was facilitated with SerialEM[83] (details can be found in Extended Data Table 2), and the cryo-EM pipeline applied for data processing is visualized in Extended Data Fig. 3. For data processing, dose-fractionated movies were first gain normalized, drift collected, summed and dose weighted using MotionCor2 (ref. 84). Motion-corrected micrographs were then imported into cryoSPARC4 (CS4)[85]. Next, the contrast transfer function (CTF) was estimated for individual summed images using Patch CTF estimation. CS4 Blob Picker was used to pick particles (no input), and particles were extracted in CS4 (box size 300). An ab initio model was generated and used as a three-dimensional (3D) template. Three rounds of heterogeneous refinements were performed using 'random phase 3D classification' in CS4 to curate the 3D model and classify [junk] and [RNAP] particles. The remaining curated particles were then refined using CS4 Local CTF refinement and polished in RELION[86,87]. Lastly, polished [RNAP] particles were refined using CS4 non-uniform refinement[88]. Nominal resolutions were determined using the gold-standard FSC 0.143 cut-off.

Model building, refinement and validation. The Mtb RNAP EC cryo-EM structure (PDB ID: 8E95)[21] was manually fitted into the cryo-EM density map using UCSF Chimera[89] as an initial model of the complex. For real space refinement, rigid body refinement was followed by all-atom refinements with Ramachandran and secondary structure restraints. Refined models were analysed and modified in Coot[90]. Quantification of orientation bias was done using CS4 orientation diagnostics[91].

Data processing, model building and structural analyses software were accessed from SBGrid[92].

Alignments

Alignments between *E. coli* RNAP bound to CBR703 (PDB ID: 4XSX) and Mtb RNAP structure bound to D-AAP1 (PDB ID: 5UHE) or AAP-SO_2 (this study; PDB ID: 9MRQ) were performed in PyMOL (v.3.03). Interactions were calculated using LIGPLOT[93] with a 3.5 Å cut-off for hydrogen bonds.

IC_{50} determination

IC_{50} values were determined using a modified version of a previously described fluorescent-aptamer-based transcription assay[46]. Upon synthesis and amplification of the gBlock described under 'Aptamer-based elongation and readthrough assay' (Extended Data Table 1), 50 nM of Mtb WT RNAP holoenzyme and CarD (2 µM) in transcription buffer (20 mM Tris-HCl pH 7.9, 50 mM KGlu, 10 mM $MgCl_2$, 1 mM DTT and 5 µg ml^{-1} bovine serum albumin) were mixed with different concentrations of MMV688845 and AAP-SO_2 (concentrations ranging from 0.01 to 10 µM). The mixtures were incubated at 37 °C for 5 min to allow for compound binding. Next, AP3 promoter–spinach DNA was added (10 nM) to each tube, and the samples were incubated for an extra 15 min at 37 °C to allow RNAP open complex formation. Then, RNAse inhibitor (0.4 U $µl^{-1}$; Thermo Fisher, EO0381) and DFHBI (Sigma-Aldrich, SML1627; 20 µM), a GFP fluorophore mimic activated by binding to spinach, were added to the mix and the reactions transferred to a flat black 384-well plate (Greiner, 781209). Transcription was initiated by adding NTPs (500 µM ATP + CTP + GTP + UTP) to each well. Next, each reaction was imaged every minute for a total of 10 min inside a Tecan Spark plate reader kept at 37 °C. Fluorescence signal was detected at 460 ± 20 nm excitation and 528 ± 20 nm emission. Relative fluorescence units were plotted against log-transformed compound concentrations in GraphPad Prism and the IC_{50} values were calculated from three independent data sets using the 'log(inhibitor) vs response – variable slope (four parameters)' function.

Generation of isogenic strains

Strains were generated as previously described[13]. Briefly, rifampicin-resistant mutants (rpoB S450L and H445Y) were isolated from five independent 5 ml H37Rv cultures (starting density of ~2,000 cells per ml) grown to stationary phase (OD_{600} > 1.5), pelleted and plated on 7H10 agar supplemented with Rif at 0.5 µg ml^{-1} (=607.57 nM). Individual colonies were then isolated, outgrown (7 days) and heat inactivated. Next, the rifampicin resistance-determining region of *rpoB*, *rpoA* and *rpoC* were amplified by PCR and Sanger sequenced, confirming the rpoB S450L and H445Y mutations, respectively.

MIC_{50-90} determinations

All compounds under investigation were dissolved in DMSO and aliquoted into a 384-well plate format using an HP D300e digital dispenser. Mtb cultures were grown to late logarithmic phase (OD_{600} ≈ 0.8) and then back diluted to a starting OD_{600} of 0.01. Of the diluted cell suspension, 50 µl was added in triplicate into wells containing the test and control compounds. Plates were incubated under static conditions at 37 °C with 5% CO_2. OD_{600} was evaluated using a Tecan Spark plate reader at day 7 post plating and percent growth was calculated relative to the DMSO vehicle control for each strain. MIC_{50} and MIC_{90} measurements were calculated using a nonlinear fit in GraphPad Prism.

Time-kill assay

All bactericidal drug experiments and growth controls were performed in duplicate at 37 °C. To determine killing kinetics, Mtb cultures (wild-type (drug-susceptible) H37Rv, rifampicin-resistant strains harbouring the S450L and H445Y mutations; see 'Generation of isogenic strains') were grown in 7H9 medium to late logarithmic phase (OD_{600} ≈ 0.8). The cultures were diluted to an OD_{600} of 0.01 in 7H9 medium supplemented with DMSO (control), 10× WT MIC_{90} (=1.38 µM) or 20× WT MIC_{90} (=2.76 µM) AAP-SO_2, 2× WT MIC_{90} (=749 nM) Fdx and/or 20× WT MIC_{90} (=243 nM) RIF. After 0, 2, 4, 10, 14, and 24 days of exposure to the compounds, the cultures were serially diluted and plated on 7H10 charcoal agar. The plates were next incubated at 37 °C for 3 weeks, and the colonies were counted to determine c.f.u. ml^{-1}.

Fluctuation assay

The fluctuation analysis was modified from previously described assays[94,95]. WT Mtb H37Rv was inoculated from a freezer stock and grown to logarithmic phase (OD_{600} ≈ 1.0). The culture was subsequently diluted into 12 independent 5 ml cultures, inoculated at 1×10^4 cells per ml. Cultures were grown in 7H9 medium supplemented with DMSO (control), 0.5× WT MIC_{90} ethambutol (EMB) (=3.67 µM) or

0.5× WT MIC_{90} AAP-SO_2 (=69 µM), and incubated under static conditions at 37 °C with 5% CO_2 until they reached stationary phase (OD_{600} ≈= 1–3). Next, 100 µl of culture from each flask was plated on 7H10 without antibiotics to determine input c.f.u. Remaining cultures were transferred to 15 ml conical tubes and collected by centrifugation at 4,000 r.p.m. for 10 min. Cultures were then resuspended in 100 µl of PBS/Tween (0.05%) and plated onto 7H10 supplemented with 20× WT MIC_{90} Rif (=0.24 µM). Plates were subsequently incubated at 37 °C for 14–21 days. Lastly, 458 colonies, approximately 15 from each plate, were isolated into 100 µl 7H9 medium supplemented with 0.5 µg ml^{-1} Rif to prevent reversion. Isolated colonies were grown out for 5–7 days and heat inactivated at 80 °C for 2 h. After heat inactivation, the rifampicin resistance-determining regions of *rpoB* were amplified by PCR and subsequently Sanger sequenced. For cultures exposed to AAP-SO_2, the AAP-SO_2 resistance-determining regions of *rpoB and rpoC* were PCR amplified and Sanger sequenced (see primers in Extended Data Table 1).

Quantification of Rif resistance rates. The observed c.f.u. on each plate without and with 20× MIC_{90} Rif (see Extended Data Table 4) were used to estimate the total number of viable cells (N_t) and Rif-resistant mutant cells (m) per ml of culture. The estimated rate of drug resistance emergence was calculated by dividing m by N_t. Statistical comparisons were performed using two-sided unpaired t-tests in GraphPad Prism. In addition, μ and its 95% confidence limits were calculated using the Lea–Coulson model ($\varepsilon < 1$) in webSalvador 0.1, setting ε to 0.99 (ref. 96). This method accounts for plating efficiency and variations in the viable cell count (N_t). Statistical comparisons were performed using the likelihood ratio test, also accounting for plating efficiency and variations in the viable cell count (N_t), through the Lea–Coulson model ($\varepsilon < 1$) comparison function implemented in webSalvador (0.1)[96].

Ex vivo rabbit caseum bactericidal activity assay

We used ex vivo rabbit caseum to assess drug potency against non-replicating Mtb, as described previously[8,58,59]. Caseum was collected from female New Zealand White rabbits (Millbrook Farm, Concord, MA) infected with Mtb HN878 via a nose-only aerosol exposure system[97,98]. The infection was allowed to progress for 16 weeks or more before necropsy. At the start of each assay, caseum was homogenized with two volumes of sterile water and bead beaten with sterile 1.4 mm ceramic beads. The potencies of RIF, Fdx and AAP-SO_2 in caseum homogenate were evaluated in 96-well plates at the final concentration range of 0.5–128 µM, both individually and in combination, at 37 °C over 7 days. A DMSO-only control well was included in each assay. To quantify bacterial burden at the start and end of the experiment, we performed serial dilutions of the caseum samples and plated them on Middlebrook 7H11 agar supplemented with 0.5% glycerol, 10% OADC and 0.4% activated charcoal to absorb drug carryover. Control and test wells were plated in triplicate. Caseum MBC_{90} was defined as the concentration of drug required to kill 90% of Mtb bacteria residing in the caseum specimen[8,58]. The bactericidal activities of the single and combined agents were plotted as the net reductions in logarithmic function of Mtb burdens per ml of caseum homogenate (Δlog(c.f.u. ml^{-1})). Synergy scores were calculated using Bliss' definition of drug independence.

Fidaxomicin stability. The stability of Fdx in rabbit caseum homogenate was assessed over 7 days. Briefly, we added 5 µM Fdx to 3-fold-diluted ex vivo rabbit caseum. Samples (20 µl) were removed immediately after Fdx addition, after 24 h and on the 7th day. Samples were extracted with 1:1 acetonitrile:methanol and analysed by liquid chromatography–tandem mass spectrometry (LC–MS/MS). We used the mass transition 1,055.19/231.00 for Fdx, and labetalol served as the internal standard. We quantified Fdx concentration in each sample and plotted the percentage recovered at each timepoint.

Statistics

All statistical analyses were conducted in GraphPad Prism (v.10.4.1), except for the fluctuation analysis which was performed using webSalvador[96].

Reporting summary

Further information on research design is available in the Nature Portfolio Reporting Summary linked to this article.

Data availability

The cryo-EM density map has been deposited in the Electron Microscopy Data Bank under accession code EMD-48561 (https://www.ebi.ac.uk/emdb/EMD-48561). The corresponding atomic coordinates have been deposited in the Protein Data Bank under accession code 9MRQ (https://www.rcsb.org/structure/9MRQ). The raw files for the native mass spectrometry experiments are available via figshare at https://doi.org/10.6084/m9.figshare.30259192 (ref. 99). All other data supporting the findings of this study are available from the corresponding author upon reasonable request. Source data are provided with this paper.

References

1. *Global Tuberculosis Report* (WHO, 2024).
2. *Clinical Overview of Latent Tuberculosis Infection* (CDC, 2024).
3. Houben, R. M. G. J. & Dodd, P. J. The global burden of latent tuberculosis infection: a re-estimation using mathematical modelling. *PLoS Med.* **13**, e1002152 (2016).
4. Ihms, E. A., Urbanowski, M. E. & Bishai, W. R. Diverse cavity types and evidence that mechanical action on the necrotic granuloma drives tuberculous cavitation. *Am. J. Pathol.* **188**, 1666–1675 (2018).
5. Saeed, W. Cavitating pulmonary tuberculosis: a global challenge. *Clin. Med. Lond. Engl.* **12**, 40–41 (2012).
6. Urbanowski, M. E., Ordonez, A. A., Ruiz-Bedoya, C. A., Jain, S. K. & Bishai, W. R. Cavitary tuberculosis: the gateway of disease transmission. *Lancet Infect. Dis.* **20**, e117–e128 (2020).
7. Pletz, M. W., Hagel, S. & Forstner, C. Who benefits from antimicrobial combination therapy? *Lancet Infect. Dis.* **17**, 677–678 (2017).
8. Sarathy, J. P. et al. Extreme drug tolerance of *Mycobacterium tuberculosis* in caseum. *Antimicrob. Agents Chemother.* **62**, e02266-17 (2018).
9. *Latent Tuberculosis Infection: Updated and Consolidated Guidelines for Programmatic Management* (WHO, 2018).
10. *Treatment Regimens for Latent TB Infection* (CDC, 2025).
11. Malenfant, J. H. & Brewer, T. F. Rifampicin mono-resistant tuberculosis—a review of an uncommon but growing challenge for global tuberculosis control. *Open Forum Infect. Dis.* **8**, ofab018 (2021).
12. Antimicrobial Resistance Collaborators. Global burden of bacterial antimicrobial resistance in 2019: a systematic analysis. *Lancet Lond. Engl.* **399**, 629–655 (2022).
13. Eckartt, K. A. et al. Compensatory evolution in NusG improves fitness of drug-resistant *M. tuberculosis*. *Nature* https://doi.org/10.1038/s41586-024-07206-5 (2024).
14. Stefan, M. A., Ugur, F. S. & Garcia, G. A. Source of the fitness defect in rifamycin-resistant *Mycobacterium tuberculosis* RNA polymerase and the mechanism of compensation by mutations in the β′ subunit. *Antimicrob. Agents Chemother.* **62**, e00164-18 (2018).
15. Campbell, E. A. et al. Structural mechanism for rifampicin inhibition of bacterial RNA polymerase. *Cell* **104**, 901–912 (2001).
16. Gagneux, S. et al. The competitive cost of antibiotic resistance in *Mycobacterium tuberculosis*. *Science* **312**, 1944–1946 (2006).
17. Labuda, S. M., Seaworth, B., Dasgupta, S. & Goswami, N. D. Bedaquiline, pretomanid, and linezolid with or without moxifloxacin for tuberculosis. *Lancet Respir. Med.* **12**, e5–e6 (2024).

18. Van Rie, A. et al. Balancing access to BPaLM regimens and risk of resistance. *Lancet Infect. Dis.* **22**, 1411–1412 (2022).
19. Bosch, B. et al. Genome-wide gene expression tuning reveals diverse vulnerabilities of *M. tuberculosis*. *Cell* **184**, 4579–4592.e24 (2021).
20. Chen, J., Boyaci, H. & Campbell, E. A. Diverse and unified mechanisms of transcription initiation in bacteria. *Nat. Rev. Microbiol.* **19**, 95–109 (2021).
21. Delbeau, M. et al. Structural and functional basis of the universal transcription factor NusG pro-pausing activity in *Mycobacterium tuberculosis*. *Mol. Cell* **83**, 1474–1488.e8 (2023).
22. Inlow, K., Tenenbaum, D., Friedman, L. J., Kondev, J. & Gelles, J. Recycling of bacterial RNA polymerase by the Swi2/Snf2 ATPase RapA. *Proc. Natl Acad. Sci. USA* **120**, e2303849120 (2023).
23. Kang, J. Y. et al. Structural basis for transcript elongation control by NusG family universal regulators. *Cell* **173**, 1650–1662.e14 (2018).
24. Kang, J. Y., Mishanina, T. V., Landick, R. & Darst, S. A. Mechanisms of transcriptional pausing in bacteria. *J. Mol. Biol.* **431**, 4007–4029 (2019).
25. Landick, R. Transcriptional pausing as a mediator of bacterial gene regulation. *Annu. Rev. Microbiol.* **75**, 291–314 (2021).
26. von Hippel, P. H. & Yager, T. D. Transcript elongation and termination are competitive kinetic processes. *Proc. Natl Acad. Sci. USA* **88**, 2307–2311 (1991).
27. Boyaci, H. et al. Fidaxomicin jams *Mycobacterium tuberculosis* RNA polymerase motions needed for initiation via RbpA contacts. *eLife* **7**, e34823 (2018).
28. Cao, X. et al. Basis of narrow-spectrum activity of fidaxomicin on *Clostridioides difficile*. *Nature* **604**, 541–545 (2022).
29. Lin, W. et al. Structural basis of transcription inhibition by fidaxomicin (Lipiarmycin A3). *Mol. Cell* **70**, 60–71.e15 (2018).
30. McClure, W. R. & Cech, C. L. On the mechanism of rifampicin inhibition of RNA synthesis. *J. Biol. Chem.* **253**, 8949–8956 (1978).
31. Lang, M. et al. Synthesis and characterization of phenylalanine amides active against *Mycobacterium abscessus* and other mycobacteria. *J. Med. Chem.* **66**, 5079–5098 (2023).
32. Lang, M. et al. Synthesis and in vitro metabolic stability of sterically shielded antimycobacterial phenylalanine amides. *ChemMedChem* **19**, e202300593 (2024).
33. Seidel, R. W., Goddard, R., Lang, M. & Richter, A. *N*α-aroyl-*N*-aryl-phenylalanine amides: a promising class of antimycobacterial agents targeting the RNA polymerase. *Chem. Biodivers.* **21**, e202400267 (2024).
34. Ballell, L. et al. Fueling open-source drug discovery: 177 small-molecule leads against tuberculosis. *ChemMedChem* **8**, 313–321 (2013).
35. Lang, M., Ganapathy, U. S., Abdelaziz, R., Dick, T. & Richter, A. Broad-spectrum in vitro activity of *N*α-aroyl-*N*-aryl-phenylalanine amides against non-tuberculous mycobacteria and comparative analysis of RNA polymerases. *Antibiotics* **13**, 404 (2024).
36. Lin, W. et al. Structural basis of *Mycobacterium tuberculosis* transcription and transcription inhibition. *Mol. Cell* **66**, 169–179.e8 (2017).
37. Artsimovitch, I., Chu, C., Lynch, A. S. & Landick, R. A new class of bacterial RNA polymerase inhibitor affects nucleotide addition. *Science* **302**, 650–654 (2003).
38. Bae, B. et al. CBR antimicrobials inhibit RNA polymerase via at least two bridge-helix cap-mediated effects on nucleotide addition. *Proc. Natl Acad. Sci. USA* **112**, E4178–E4187 (2015).
39. Feng, Y. et al. Structural basis of transcription inhibition by CBR hydroxamidines and CBR pyrazoles. *Structure* **23**, 1470–1481 (2015).
40. Olinares, P. D. B. et al. Native mass spectrometry-based screening for optimal sample preparation in single-particle cryo-EM. *Structure* **29**, 186–195.e6 (2021).
41. Mann, L. et al. In vitro profiling of the synthetic RNA polymerase inhibitor MMV688845 against *Mycobacterium abscessus*. *Microbiol. Spectr.* **10**, e0276022 (2022).
42. Belogurov, G. A. & Artsimovitch, I. The mechanisms of substrate selection, catalysis, and translocation by the elongating RNA polymerase. *J. Mol. Biol.* **431**, 3975–4006 (2019).
43. Gnatt, A. L., Cramer, P., Fu, J., Bushnell, D. A. & Kornberg, R. D. Structural basis of transcription: an RNA polymerase II elongation complex at 3.3 Å resolution. *Science* **292**, 1876–1882 (2001).
44. Korzheva, N. et al. A structural model of transcription elongation. *Science* **289**, 619–625 (2000).
45. Zhang, J. & Landick, R. in *RNA Polymerases as Molecular Motors* (eds Buc, H. & Strick, T.) 206–235 (The Royal Society of Chemistry, 2009).
46. Jensen, D. et al. High-throughput, fluorescent-aptamer-based measurements of steady-state transcription rates for the *Mycobacterium tuberculosis* RNA polymerase. *Nucleic Acids Res.* **51**, e99 (2023).
47. Jovanovic, M. et al. Activity map of the *Escherichia coli* RNA polymerase bridge helix. *J. Biol. Chem.* **286**, 14469–14479 (2011).
48. Kennedy, S. R. & Erie, D. A. Templated nucleoside triphosphate binding to a noncatalytic site on RNA polymerase regulates transcription. *Proc. Natl Acad. Sci. USA* **108**, 6079–6084 (2011).
49. Miropolskaya, N., Artsimovitch, I., Klimasauskas, S., Nikiforov, V. & Kulbachinskiy, A. Allosteric control of catalysis by the F loop of RNA polymerase. *Proc. Natl Acad. Sci. USA* **106**, 18942–18947 (2009).
50. Miropolskaya, N., Nikiforov, V., Klimasauskas, S., Artsimovitch, I. & Kulbachinskiy, A. Modulation of RNA polymerase activity through the trigger loop folding. *Transcription* **1**, 89–94 (2010).
51. Miropolskaya, N. et al. Interplay between the trigger loop and the F loop during RNA polymerase catalysis. *Nucleic Acids Res.* **42**, 544–552 (2014).
52. Borrell, S. et al. Reference set of *Mycobacterium tuberculosis* clinical strains: a tool for research and product development. *PLoS ONE* **14**, e0214088 (2019).
53. Mariam, D. H., Mengistu, Y., Hoffner, S. E. & Andersson, D. I. Effect of rpoB mutations conferring rifampin resistance on fitness of *Mycobacterium tuberculosis*. *Antimicrob. Agents Chemother.* **48**, 1289–1294 (2004).
54. Sander, P. et al. Fitness cost of chromosomal drug resistance-conferring mutations. *Antimicrob. Agents Chemother.* **46**, 1204–1211 (2002).
55. Jin, D. J., Walter, W. A. & Gross, C. A. Characterization of the termination phenotypes of rifampicin-resistant mutants. *J. Mol. Biol.* **202**, 245–253 (1988).
56. Takayama, K. & Kilburn, J. O. Inhibition of synthesis of arabinogalactan by ethambutol in *Mycobacterium smegmatis*. *Antimicrob. Agents Chemother.* **33**, 1493–1499 (1989).
57. Luria, S. E. & Delbrück, M. Mutations of bacteria from virus sensitivity to virus resistance. *Genetics* **28**, 491–511 (1943).
58. Sarathy, J. P. et al. A novel tool to identify bactericidal compounds against vulnerable targets in drug-tolerant *M. tuberculosis* found in caseum. *mBio* **14**, e0059823 (2023).
59. Ashwath, P., Osiecki, P., Weiner, D., Via, L. E. & Sarathy, J. P. Role of DNA double-strand break formation in gyrase inhibitor-mediated killing of nonreplicating persistent *Mycobacterium tuberculosis* in caseum. *ACS Infect. Dis.* **10**, 3631–3639 (2024).
60. Bliss, C. I. The calculation of microbial assays. *Bacteriol. Rev.* **20**, 243–258 (1956).
61. Abd El-Hafeez, T., Shams, M. Y., Elshaier, Y. A. M. M., Farghaly, H.M. & Hassanien, A. E. Harnessing machine learning to find synergistic combinations for FDA-approved cancer drugs. *Sci. Rep.* **14**, 2428 (2024).

62. Baym, M., Stone, L. K. & Kishony, R. Multidrug evolutionary strategies to reverse antibiotic resistance. *Science* **351**, aad3292 (2016).
63. Rasouly, A. et al. Analysing the fitness cost of antibiotic resistance to identify targets for combination antimicrobials. *Nat. Microbiol.* **6**, 1410–1423 (2021).
64. Roemhild, R. & Andersson, D. I. Mechanisms and therapeutic potential of collateral sensitivity to antibiotics. *PLoS Pathog.* **17**, e1009172 (2021).
65. Szybalski, W. & Bryson, V. Genetic studies on microbial cross resistance to toxic agents. I. Cross resistance of *Escherichia coli* to fifteen antibiotics. *J. Bacteriol.* **64**, 489–499 (1952).
66. *Xpert MTB/RIF Assay* (CDC, 2024).
67. *Molecular Detection of Drug Resistance (MDDR) in Mycobacterium tuberculosis Complex by DNA Sequencing User Guide* (CDC, 2024).
68. Kupcova, K. et al. Vertical targeting of the PI3K/AKT pathway at multiple points is synergistic and effective for non-Hodgkin lymphoma. *Exp. Hematol. Oncol.* **13**, 108 (2024).
69. Ryan, M. B. et al. Vertical Pathway inhibition overcomes adaptive feedback resistance to KRASG12C inhibition. *Clin. Cancer Res.* **26**, 1633–1643 (2020).
70. Woo, S.-U. et al. Vertical inhibition of the PI3K/Akt/mTOR pathway is synergistic in breast cancer. *Oncogenesis* **6**, e385 (2017).
71. Reissig, T. M. et al. Lasting response by vertical inhibition with cetuximab and trametinib in KRAS-mutated colorectal cancer patient-derived xenografts. *Mol. Oncol.* **17**, 2396–2414 (2023).
72. Masters, P. A., O'Bryan, T. A., Zurlo, J., Miller, D. Q. & Joshi, N. Trimethoprim-sulfamethoxazole revisited. *Arch. Intern. Med.* **163**, 402–410 (2003).
73. Minato, Y. et al. Mutual potentiation drives synergy between trimethoprim and sulfamethoxazole. *Nat. Commun.* **9**, 1003 (2018).
74. Noeske, J. et al. Synergy of streptogramin antibiotics occurs independently of their effects on translation. *Antimicrob. Agents Chemother.* **58**, 5269–5279 (2014).
75. Dartois, V. A. & Rubin, E. J. Anti-tuberculosis treatment strategies and drug development: challenges and priorities. *Nat. Rev. Microbiol.* **20**, 685–701 (2022).
76. Hubin, E. A. et al. Structural, functional, and genetic analyses of the actinobacterial transcription factor RbpA. *Proc. Natl Acad. Sci. USA* **112**, 7171–7176 (2015).
77. Srivastava, D. B. et al. Structure and function of CarD, an essential mycobacterial transcription factor. *Proc. Natl Acad. Sci. USA* **110**, 12619–12624 (2013).
78. Davis, E., Chen, J., Leon, K., Darst, S. A. & Campbell, E. A. Mycobacterial RNA polymerase forms unstable open promoter complexes that are stabilized by CarD. *Nucleic Acids Res.* **43**, 433–445 (2015).
79. Olinares, P. D. B. & Chait, B. T. Native mass spectrometry analysis of affinity-captured endogenous yeast RNA exosome complexes. *Methods Mol. Biol.* **2062**, 357–382 (2020).
80. Marty, M. T. et al. Bayesian deconvolution of mass and ion mobility spectra: from binary interactions to polydisperse ensembles. *Anal. Chem.* **87**, 4370–4376 (2015).
81. Reid, D. J. et al. MetaUniDec: high-throughput deconvolution of native mass spectra. *J. Am. Soc. Mass. Spectrom.* **30**, 118–127 (2019).
82. Czyz, A., Mooney, R. A., Iaconi, A. & Landick, R. Mycobacterial RNA polymerase requires a U-tract at intrinsic terminators and is aided by NusG at suboptimal terminators. *mBio* **5**, e00931 (2014).
83. Mastronarde, D. N. Automated electron microscope tomography using robust prediction of specimen movements. *J. Struct. Biol.* **152**, 36–51 (2005).
84. Zheng, S. Q. et al. MotionCor2: anisotropic correction of beam-induced motion for improved cryo-electron microscopy. *Nat. Methods* **14**, 331–332 (2017).
85. Punjani, A., Rubinstein, J. L., Fleet, D. J. & Brubaker, M. A. cryoSPARC: algorithms for rapid unsupervised cryo-EM structure determination. *Nat. Methods* **14**, 290–296 (2017).
86. Scheres, S. H. W. RELION: implementation of a Bayesian approach to cryo-EM structure determination. *J. Struct. Biol.* **180**, 519–530 (2012).
87. Zivanov, J. et al. New tools for automated high-resolution cryo-EM structure determination in RELION-3. *eLife* **7**, e42166 (2018).
88. Baldwin, P. R. & Lyumkis, D. Non-uniformity of projection distributions attenuates resolution in cryo-EM. *Prog. Biophys. Mol. Biol.* **150**, 160–183 (2020).
89. Pettersen, E. F. et al. UCSF Chimera—a visualization system for exploratory research and analysis. *J. Comput. Chem.* **25**, 1605–1612 (2004).
90. Emsley, P. & Cowtan, K. Coot: model-building tools for molecular graphics. *Acta Crystallogr. D Biol. Crystallogr.* **60**, 2126–2132 (2004).
91. Tan, Y. Z. et al. Addressing preferred specimen orientation in single-particle cryo-EM through tilting. *Nat. Methods* **14**, 793–796 (2017).
92. Morin, A. et al. Collaboration gets the most out of software. *eLife* **2**, e01456 (2013).
93. Wallace, A. C., Laskowski, R. A. & Thornton, J. M. LIGPLOT: a program to generate schematic diagrams of protein–ligand interactions. *Protein Eng.* **8**, 127–134 (1995).
94. Ford, C. B. et al. Use of whole genome sequencing to estimate the mutation rate of *Mycobacterium tuberculosis* during latent infection. *Nat. Genet.* **43**, 482–486 (2011).
95. Ford, C. B. et al. *Mycobacterium tuberculosis* mutation rate estimates from different lineages predict substantial differences in the emergence of drug-resistant tuberculosis. *Nat. Genet.* **45**, 784–790 (2013).
96. Zheng, Q. webSalvador: a web tool for the Luria-Delbrük experiment. *Microbiol. Resour. Announc.* **10**, e00314–e00321 (2021).
97. Subbian, S. et al. Chronic pulmonary cavitary tuberculosis in rabbits: a failed host immune response. *Open Biol.* **1**, 110016 (2011).
98. Via, L. E. et al. Tuberculous granulomas are hypoxic in guinea pigs, rabbits, and nonhuman primates. *Infect. Immun.* **76**, 2333–2340 (2008).
99. Bosch, B. et al. Transcription co-inhibition reduces rifampicin resistance and enhances *M. tuberculosis* granuloma clearance, native mass spectrometry datasets. *Figshare* https://doi.org/10.6084/m9.figshare.30259192 (2025).
100. Peek, J. et al. Rifamycin congeners kanglemycins are active against rifampicin-resistant bacteria via a distinct mechanism. *Nat. Commun.* **9**, 4147 (2018).
101. Lea, D. E. & Coulson, C. A. The distribution of the numbers of mutants in bacterial populations. *J. Genet.* **49**, 264–285 (1949).
102. Zheng, S. et al. SynergyFinder Plus: toward better interpretation and annotation of drug combination screening datasets. *Genomics Proteomics Bioinformatics* **20**, 587–596 (2022).
103. Liebschner, D. et al. Macromolecular structure determination using X-rays, neutrons and electrons: recent developments in Phenix. *Acta Crystallogr. D Struct. Biol.* **75**, 861–877 (2019).
104. Heymann, J. B. Guidelines for using Bsoft for high resolution reconstruction and validation of biomolecular structures from electron micrographs. *Protein Sci.* **27**, 159–171 (2018).
105. Cardone, G., Heymann, J. B. & Steven, A. C. One number does not fit all: mapping local variations in resolution in cryo-EM reconstructions. *J. Struct. Biol.* **184**, 226–236 (2013).

Acknowledgements
We thank members of the Campbell and Darst labs. We thank S. Darst for his discussion and comments on the manuscript. P.D.B.O. thanks B. Chait for guidance and support. This work was supported by R35 GM151879 (E.A.C.), The Black Family Therapeutic Development Fund (E.A.C.), and the SNF RU Institute for Global Infectious Disease Research at The Rockefeller University (P.D.B.O., J.M.R. and E.A.C.). B.B. was supported by the National Center for Advancing Translational Sciences, National Institutes of Health, through Rockefeller University, Grant # UL1 TR001866. This research was also supported in part by NIH T32 GM136640-Tan to M.S.; by a joint NIH Tuberculosis Research Units Network (TBRU-N) grant (U19AI162584, J.M.R.); and by funding from the Deutsche Forschungsgemeinschaft (DFG, German Research Foundation) – project number 432291016 (A.R.) and Mukoviszidose Institut gGmbH (Bonn, Germany; the research and development arm of the German Cystic Fibrosis Association Mukoviszidose e. V.) – project number 2202 (A.R.).

Author contributions
B.B., E.A.C. and J.M.R. conceptualized the project. B.B., V.M.-G., M. Lilic, P.D.B.O., J.S., K.A.E., M. Lang, M.S., A.R., P.N., J.M.R. and E.A.C. conducted investigations. B.B., V.M.-G., M. Lilic, P.D.B.O., M.S., J.S., P.N., J.M.R. and E.A.C. performed data analysis. B.B. and E.A.C. wrote the original manuscript draft. A.R., J.M.R. and E.A.C. acquired funding. J.M.R. and E.A.C. supervised the project. All authors contributed to writing, reviewing and editing the manuscript.

Competing interests
The authors declare no competing interests.

Additional information
Extended data is available for this paper at https://doi.org/10.1038/s41564-025-02201-6.

Supplementary information The online version contains supplementary material available at https://doi.org/10.1038/s41564-025-02201-6.

Correspondence and requests for materials should be addressed to Barbara Bosch, Jeremy M. Rock or Elizabeth A. Campbell.

Peer review information *Nature Microbiology* thanks Anthony Baughn, Konstantin Brodolin, Michael Niederweis and the other, anonymous, reviewer(s) for their contribution to the peer review of this work.

Reprints and permissions information is available at www.nature.com/reprints.

Publisher's note Springer Nature remains neutral with regard to jurisdictional claims in published maps and institutional affiliations.

[1]Laboratory of Molecular Pathogenesis, The Rockefeller University, New York, NY, USA. [2]Laboratory of Host–Pathogen Biology, The Rockefeller University, New York, NY, USA. [3]Center for Discovery and Innovation, Hackensack Meridian Health, Nutley, NJ, USA. [4]Hackensack Meridian School of Medicine, Department of Medical Sciences, Nutley, NJ, USA. [5]Laboratory of Mass Spectrometry and Gaseous Ion Chemistry, The Rockefeller University, New York, NY, USA. [6]Institute of Pharmacy, Martin-Luther-University Halle-Wittenberg, Halle, Germany. [7]Tri-Institutional Program in Chemical Biology, The Rockefeller University, New York, NY, USA. [8]These authors contributed equally: Barbara Bosch, Vanisha Munsamy-Govender. [9]These authors jointly supervised this work: Jeremy M. Rock, Elizabeth A. Campbell. ✉e-mail: bbosch@rockefeller.edu; rock@rockefeller.edu; campbee@rockefeller.edu

https://doi.org/10.1038/s41564-025-02201-6

Extended Data Table 1 | Oligonucleotides, Primers and plasmids used

Oligonucleotides	
EC T-DNA for assay	5′-CCGGCATGAGAGGGTATTCGCCGCGTACCT CTCCTAGCCCGCAAGTATCCGACG-3′
EC NT-DNA for assay	5′-CGTCGGATACTTGCGGGCTAGCCTCTTTTCGCG GCGAATACCCTCTCATGCCGG-3′
EC RNA for assay	5′-FAM-ACAUUCAAAGCGGAGAGGUA-3′
EC RNA for structure	5′-GCAUUCAAAGCGGAGAGGUA-3′
EC T-DNA for structure	5′-CCGGCATGAGAGGGTATTCGCCGCCTACCT CTCCTAGCCCGCAAGTATCCGACG-3′
EC NT-DNA for structure	5′-CGTCGGATACTTGCGGGCTAGCCTCTTTTGGCG GCGAATACCCTCTCATGCCGG-3′
gBlock for aptamer-based assays	5′CCGTTGAATAGTAAAACGACGGCCAGGAGCTCGGTACCCGGGGATCATCTATGGATGACCGAACCTGGTCTTGACTCCATTG CCGGATTTGTATTAGACTGGCAGGGTTGGATGGATGAGATTTGAAGGTTGGGTGACGCGACCGAAATGGTGAAGGACGGGTCCA GTGCTTCGGCACTGTTGAGTAGAGTGTGAGCTCCGTAACTGGTCGCGTCCCCACCTGACCCCATGCCGAACTCAGAAGTGAAACG CCGTAGCGCCGATGGTAGTGTGGGGTCTCCCCATGCGAGAGTAGGGAACTGCCAGGATCCAGGACACCGCCGAACATACAAA AACACCCCCGGTAACGGTGGTGTTTTTGTATGTTTATATCGACCGTGCTGGCTCCCTCCCCTCCTCTCCGCTCTGCCGCTCA GCCGCTCGCGCCATGGACGCTCTCCTGAGTAGGACAAATCCGCCGGGAGCGGATTTGAACGTTGCGAAGCAACGTCATAGCTG TTTCCTGGCAAGACGTT-3′
Primers	
rpoB Rif-resistant Forward	5′-GTACGGTCGGCGAGCTGATC-3′
rpoB Rif-resistant Reverse	5′-CCTCGTCGGCGGTCAGGTAC-3′
rpoB AAP-SO_2 R Forward	5′-GTACGGTCGGCGAGCTGATC-3′
rpoB AAP-SO_2 R Reverse	5′-gcctggcgctgcatgtttg-3′
rpoB sequencing primer	5′-GGGTCGGCATGTCGCGGATG-3′
rpoC AAP-SO_2 R Forward	5′-gcgttacccgatgatcgtggtc-3′
rpoC AAP-SO_2 R Reverse	5′-tgaccacgctcgacgatgac-3′
rpoC sequencing primer	5′-gtggagatttggaaggaagccac-3′
M13 Forward	5′-GTAAAACGACGGCCAG-3′
M13 Reverse	5′-CAGGAAACAGCTATGAC-3′
Plasmids	
pMP61	Mtb WT RNAP overexpression plasmid. rpoB and rpoC linked. His8 tag at rpoBC - C terminal (Lab stock # 5842) as previously reported[27]
pET SUMO	Mtb CarD overexpression plasmid with 10xHis-tag on N-terminus as previously reported[78]
pET20b	Mtb RbpA overexpression plasmid as previously reported[76]
pAC27	Mtb σA overexpression plasmid. 12xHis-tag on N-terminus as previously reported[13]
pJC1	Plasmid for generation of termination assay scaffold[103]

https://doi.org/10.1038/s41564-025-02201-6

Extended Data Table 2 | Cryo-EM data collection, model refinement and validation statistics

	MtbEC AAP-SO_2
	PDB: 9MRQ (EMD-48561)
Data collection and processing	
Magnification	81000
Voltage (kV)	300
Electron exposure (e-/Å2)	50.5
Defocus range (μm)	1.0 to 2.5
Pixel size (Å)	1.09
Symmetry imposed	C1
Initial particle images (no.)	8,712,992
Final particle images (no.)	347,600
Map resolution (Å) FSC threshold 0.143	2.97
Map resolution range (Å)	2.5-7
Refinement	
Initial model used (PDB code)	8E95
Model resolution range (Å)	2.5-7
Map sharpening B factor (A2)	115.9
Model resolution (Å) FSC threshold 0.5	3.1
Model composition	
Non-hydrogen atoms	23,940
Protein residues	2,909
Nucleic acid residues	61
Ligands	4 (Zn: 2 - Mg: 1 – AAP-SO_2 (BBL): 1)
B factors (A^2)	
Protein	51.84
Nucleic acid	90.57
Ligands	47.82
R.m.s. deviations	
Bond lengths (Å)	0.003
Bond angles (o)	0.493
Validation	
MolProbity score	1.69
Clashscore	4.54
Poor rotamers (%)	1.68
Ramachandran plot[i]	
Favored (%)	95.75
Allowed (%)	4.08
Outliers (%)	0.17

[i] Ramachandran plot parameters calculated in PHENIX[103].

https://doi.org/10.1038/s41564-025-02201-6

Extended Data Table 3 | Absolute values of Termination Efficiency calculations per gel

Repeat 1				
Condition	**Mean**	**Area**	**Background-corrected Mean**	**Termination efficiency**
WT 60′ - RO	143.344	0.34	138.08	0.52785091
WT 60′ - Term	159.634	0.34	154.37	
WT 60′ + AAP-SO_2 - RO	13.505	0.34	8.241	0.93676578
WT 60′ + AAP-SO_2 - Term	127.348	0.34	122.084	
S450L 60′ - RO	45.732	0.34	40.468	0.79354536
S450L 60′ - Term	160.81	0.34	155.546	
S450L 60′ + AAP-SO_2 - RO	6.88	0.34	1.616	0.98199483
S450L 60′ + AAP-SO_2 - Term	93.4	0.34	88.136	
Gel background	5.264	0.34	0	
Repeat 2				
Condition	**Mean**	**Area**	**Background-corrected Mean**	**Termination efficiency**
WT 60′ - RO	105.834	0.34	100.57	0.58129853
WT 60′ - Term	144.889	0.34	139.625	
WT 60′ + AAP-SO_2 - RO	14.126	0.34	8.862	0.93395439
WT 60′ + AAP-SO_2 - Term	130.582	0.34	125.318	
S450L 60′ - RO	46.864	0.34	41.6	0.78849214
S450L 60′ - Term	160.347	0.34	155.083	
S450L 60′ + AAP-SO_2 - RO	6.21	0.34	0.946	0.99022111
S450L 60′ + AAP-SO_2 - Term	101.057	0.34	95.793	
Gel background	5.264	0.34	0	
Repeat 3				
Condition	**Mean**	**Area**	**Background-corrected Mean**	**Termination efficiency**
WT 60′ - RO	777.806	0.216	752.631	0.31007301
WT 60′ - Term	363.429	0.216	338.254	
WT 60′ + AAP-SO_2 - RO	159.041	0.216	133.866	0.81969525
WT 60′ + AAP-SO_2 - Term	633.752	0.216	608.577	
S450L 60′ - RO	238.848	0.216	213.673	0.4830888
S450L 60′ - Term	224.867	0.216	199.692	
S450L 60′ + AAP-SO_2 - RO	43.583	0.216	18.408	0.95465362
S450L 60′ + AAP-SO_2 - Term	412.709	0.216	387.534	
Gel background	25.175	0.216	0	

https://doi.org/10.1038/s41564-025-02201-6

Extended Data Table 4 | Fluctuation analysis per condition

DMSO	CFU(50 µL of 10^-6 dilution)	CFU/mL	CFU Rif-resistant (5mL)	CFU Rif-resistant /mL	Rif-resistance Freq
1	69	1.38E+09	25	5	3.62E-09
2	53	1.06E+09	53	10.6	1.00E-08
3	62	1.24E+09	30	6	4.84E-09
4	70	1.40E+09	79	15.8	1.13E-08
5	65	1.30E+09	66	13.2	1.02E-08
6	60	1.20E+09	52	10.4	8.67E-09
7	55	1.10E+09	25	5	4.55E-09
8	91	1.82E+09	60	12	6.59E-09
9	63	1.26E+09	35	7	5.56E-09
10	74	1.48E+09	47	9.4	6.35E-09
11	52	1.04E+09	26	5.2	5.00E-09
12	65	1.30E+09	56	11.2	8.62E-09
Total					
MEAN		1.30E+09			7.10E-09
	5 mL of culture	6.49E+09		**Median**	**6.47E-09**
			Inf limit	**µ Rif**	**Sup limit**
			1.46E-09	2.02E-09	2.63E-09
			ε		
			0.99		
0.5X MIC_{90} AAP-SO_2	**CFU 50 of 10-6**	**CFU/mL**	**CFU Rif-resistance 5mL**	**Rif/mL**	**Rif-resistance Freq**
1	43	8.60E+08	20	4	4.65E-09
2	64	1.28E+09	10	2	1.56E-09
3	63	1.26E+09	20	4	3.17E-09
4	57	1.14E+09	16	3.2	2.81E-09
5	16	3.20E+08	8	1.6	5.00E-09
6	69	1.38E+09	17	3.4	2.46E-09
7	152	3.04E+09	20	4	1.32E-09
8	99	1.98E+09	23	4.6	2.32E-09
9	112	2.24E+09	17	3.4	1.52E-09
10	67	1.34E+09	6	1.2	8.96E-10
11	36	7.20E+08	3	0.6	8.33E-10
12	162	3.24E+09	11	2.2	6.79E-10
Total					
MEAN		1.57E+09			2.27E-09
	5 mL of culture	7.83E+09		**Median**	**1.94E-09**
			Inf limit	**µ Rif**	**Sup limit**
			4.38E-10	6.67E-10	9.33E-10
			ε		
			0.99		
0.5X MIC_{90} EMB	**CFU 50 µL of 10-6**	**CFU/mL**	**CFU Rif-resistance 5mL**	**Rif/mL**	**Rif-resistance Freq**
1	59	1.18E+09	17	3.4	2.88E-09
2	63	1.26E+09	43	8.6	6.83E-09
3	54	1.08E+09	13	2.6	2.41E-09
4	68	1.36E+09	40	8	5.88E-09
5	52	1.04E+09	42	8.4	8.08E-09
6	64	1.28E+09	30	6	4.69E-09
7	60	1.20E+09	23	4.6	3.83E-09

https://doi.org/10.1038/s41564-025-02201-6

Extended Data Table 4 (continued) | Fluctuation analysis per condition

DMSO	CFU(50 µL of 10^-6 dilution)	CFU/mL	CFU Rif-resistant (5mL)	CFU Rif-resistant /mL	Rif-resistance Freq
8	61	1.22E+09	31	6.2	5.08E-09
9	125	2.50E+09	65	13	5.20E-09
10	59	1.18E+09	28	5.6	4.75E-09
11	59	1.18E+09	29	5.8	4.92E-09
12	52	1.04E+09	11	2.2	2.12E-09
Total					
MEAN		1.29E+09			4.72E-09
	5 mL of culture	6.47E+09		**Median**	**4.83E-09**
			Inf limit	**µ RIF**	**Sup limit**
			9.93e-10	1.43e-09	1.91E-09
			0.99		

https://doi.org/10.1038/s41564-025-02201-6

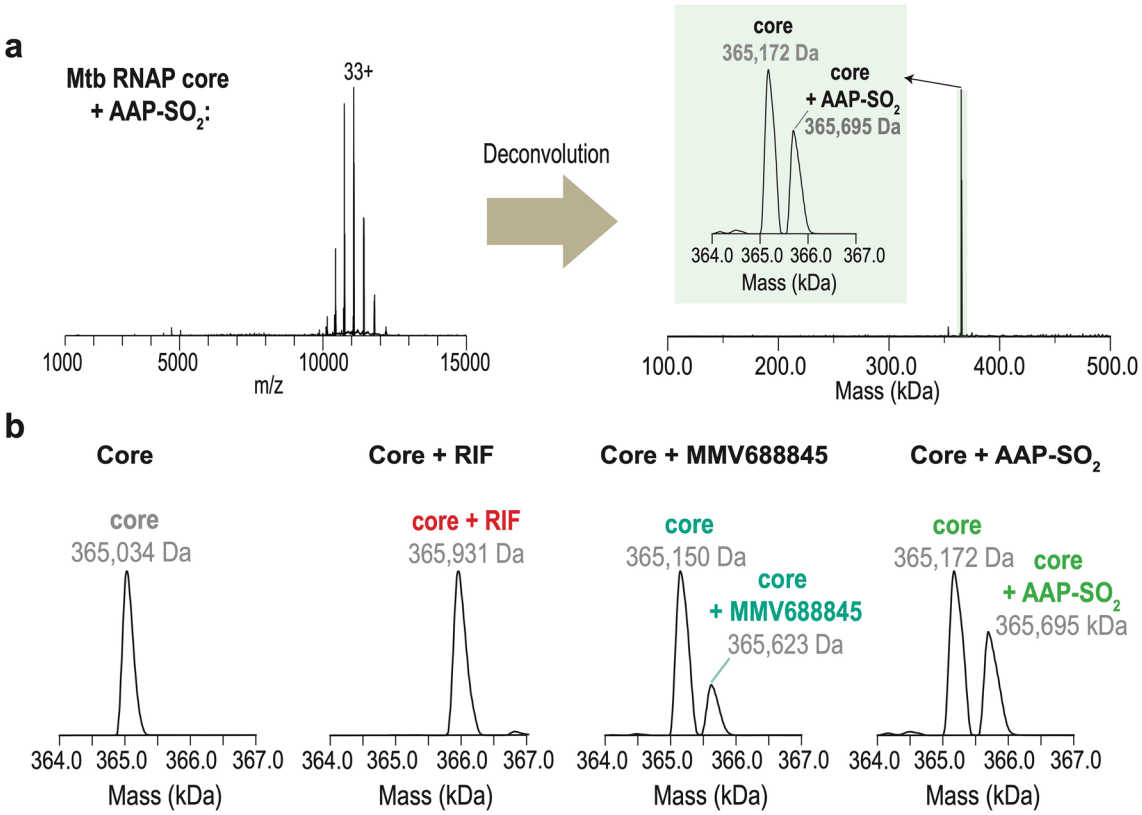

Extended Data Fig. 1 | Native mass spectrometry data processing, deconvolution, and mass measurements. a, Data processing and deconvolution of native mass spectrometry spectra using the UniDec software[80,81]. Analysis of a representative native mass spectrometry spectrum (sample: Mtb RNAP core + AAP-SO_2) is shown. **b**, Mass measurements obtained from UniDec deconvolution of the native mass spectrometry data for Mtb core samples incubated with Rif, MMV688845 and AAP-SO_2. The RNAP core complex is a heteropentameric complex comprised of α2ββ'ω. The expected masses for the complexes are RNAP core: 365,088 Da, core + Rif: 365,911 Da, core + MMV688845: 365,523 Da and core + AAP-SO_2: 365,583 Da. The mass deviation from expected mass across all the native mass spectrometry measurements ranged from 0.006 – 0.03%.

https://doi.org/10.1038/s41564-025-02201-6

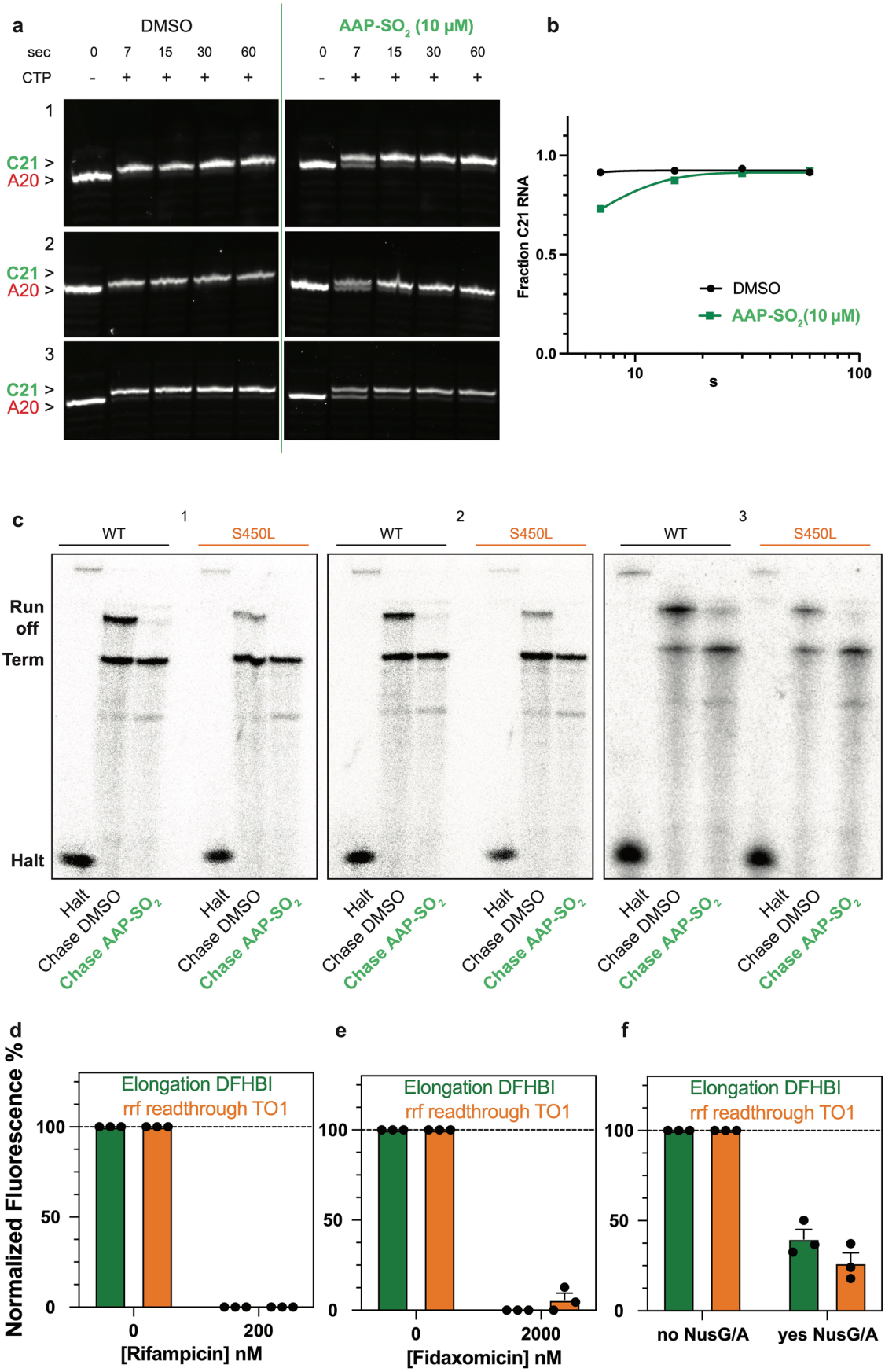

Extended Data Fig. 2 | See next page for caption.

https://doi.org/10.1038/s41564-025-02201-6

Extended Data Fig. 2 | Replicates of the AAP-SO_2 elongation and termination assays. a, Urea-page gels showing the fraction of C21 RNA formed at specific time points (0, 7, 15, 30, and 60 s) in the presence of DMSO (control) or AAP-SO_2 for each of the 3 experimental replicates. **b**, Quantification of the apparent nucleotide addition rate in the absence (DMSO) and presence of AAP-SO_2 (10 mM) over time. AAP-SO_2 reduces the rate of NTP incorporation by 2.9-fold. Data are represented as (mean ± s.d.; $n = 3$). **c**, Urea-page gels showing the Mtb RNAP *in vitro* termination assay on a promoter-initiated template in the presence or absence of AAP-SO_2 for each of the 3 experimental replicates. **d-f**, Percent fluorescence observed in the elongation (green) and readthrough channel (orange) in the presence of (**d**) 200 nM rifampicin, (**e**) 2000 nM fidaxomicin or (**f**) 1000 nM NusG and NusA versus in the DMSO (**d**,**e**) or no factor control (**f**) (mean ± s.e.m.; $n = 3$).

https://doi.org/10.1038/s41564-025-02201-6

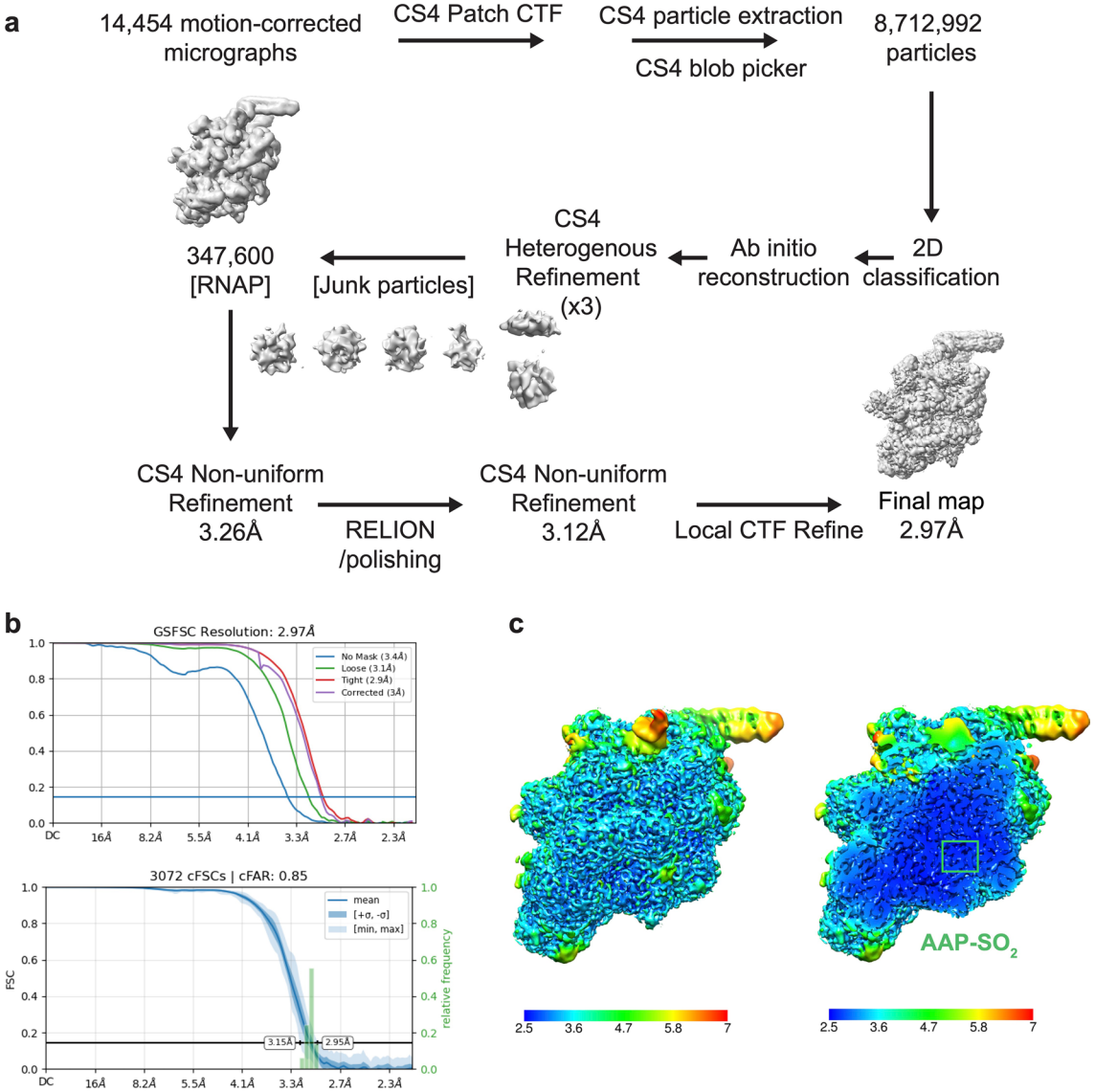

Extended Data Fig. 3 | Data processing workflow and cryo-EM map validation for MtbEC with AAP-SO_2. **a**, Cryo-EM pipeline applied for data processing of MtbEC with AAP-SO_2. Dose-fractionated movies (14,454) were frame aligned and summed using MotionCor2[84]. Motion-corrected micrographs were then imported into cryoSPARC4 (CS4)[85]. CTFs were estimated by Patch CTF, and CS4 Blob Picker was used to pick and extract particles. Next, particles were curated using 3 rounds of CS4 heterogeneous refinement (6 classes each) and unwanted particles [junk particles] were removed. The remaining particles [RNAP] (n = 347.6k) were polished in RELION[86,87] and refined with CS4 non-uniform refinement. Lastly, local CTF refinement was performed on curated particles to get the final map. **b**, Quantification of orientation bias using gold standard FSC (red line) and conical FSC (cFSC) of MtbEC with AAP-SO_2, generated with CS4 orientation diagnostics[91], indicate minimal orientation bias and a conical FSC Area Ratio (cFAR) of 0.85, **c**, Maps representing the local resolution calculations, generated using blocres from the Bsoft package[104,105]. The green box indicates the binding pocket of AAP-SO_2 and shows the local resolution (2.5 Å) in that area.

https://doi.org/10.1038/s41564-025-02201-6

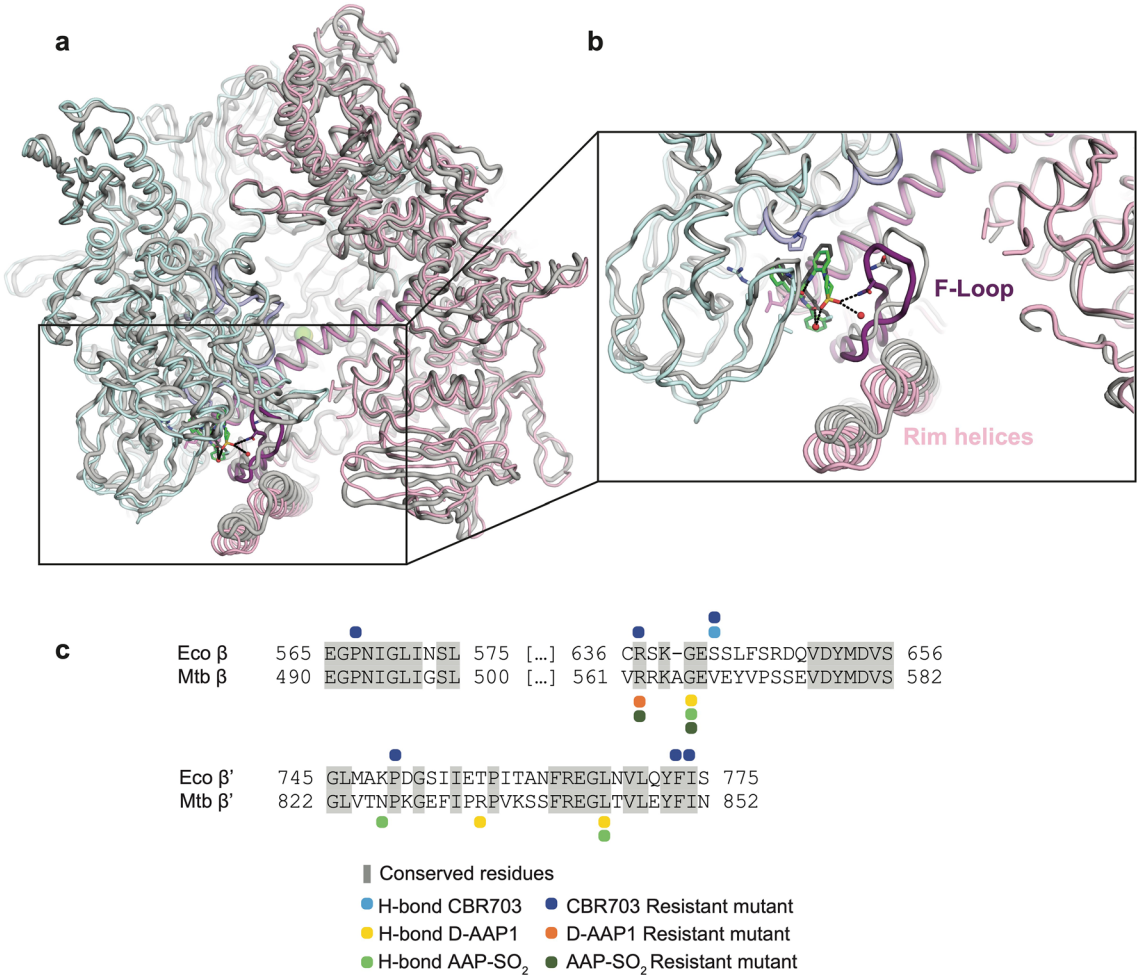

Extended Data Fig. 4 | Differences between CBR703, D-AAP1 and AAP-SO_2 binding. a, Overall alignment between Mtb RNAP structure bound to D-AAP1 (5UHE; grey)[36] and AAP-SO_2 (in color). Global RMSD is 1.142 Å over 2557 atoms. **b**, Alignment of the rim helices and F-loop region upon D-AAP1 (grey) versus AAP-SO_2 (in color) binding. RMSD of the rim helices and F-loop between the two structures is 2.69 Å over 82 Cα atoms. **c**, Sequence variation between the Mtb and *Eco* binding pockets. Conserved residues are highlight in grey. Hydrogen bonds (H-bonds) between CBR703 and *E. coli* (light blue) as well as between D-AAP1 (yellow) and AAP-SO_2 (light green) are dotted. Interactions were calculated using LIGPLOT[93] with a 3.5 Å cut-off for hydrogen bonds. **c**, Residues conferring resistance to CBR703, D-AAP1 and AAP-SO_2 (this study) are indicated in dark blue, orange and green respectively. Alignments were performed in PyMOL (The PyMOL Molecular Graphics System, Version 3.03 Schrödinger, LLC).

https://doi.org/10.1038/s41564-025-02201-6

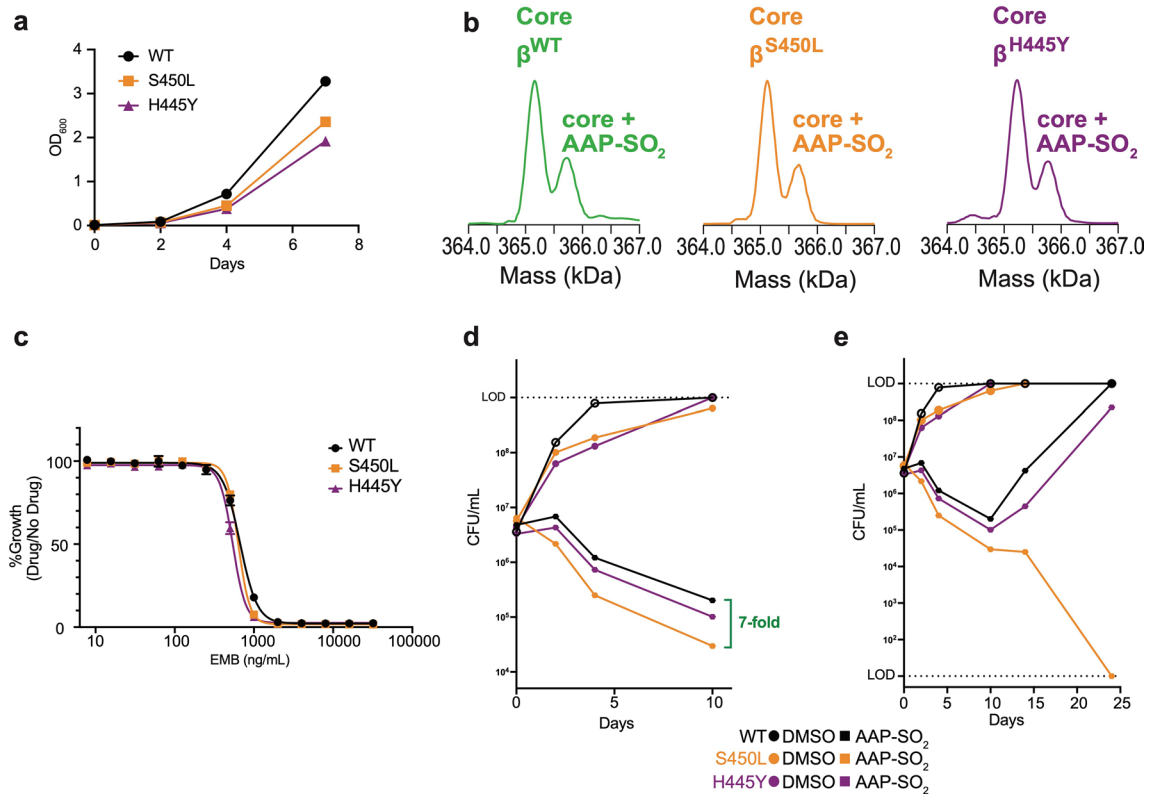

Extended Data Fig. 5 | AAP-SO_2 binds Rif-resistant and WT RNAP similarly but affect WT, βS450L and βH445Y Mtb differentially. a, Growth of isogenic WT H37Rv and βS450L and βH445Y mutant strains in drug-free conditions. **b**, Native mass spectrometry analysis of WT, βS450L and βH445Y RNAP core bound to AAP-SO_2. **c**, MIC assay for EMB. MIC_{50} values for WT, βS450L, and βH445Y are 667.9 ± 17.3, 633.0 ± 12.7, and 540.0 ± 8.2 ng/ml, respectively (= 3.27 ± 0.08, 3.10 ± 0.06, 2.64 ± 0.04 μM). Data are mean ± s.e.m. (n = 3). **d**, Time-kill experiment showing the effect of DMSO and AAP-SO_2 on WT H37Rv, βS450L, and βH445Y strains over 10 days of exposure. Data are from duplicate biological cultures treated with AAP-SO_2 at 1.38 μM. **e**, Time-kill experiment showing the development of resistance to AAP-SO_2 (1.38 μM) in duplicate WT, βS450L, and βH445Y strains over 24 days.

https://doi.org/10.1038/s41564-025-02201-6

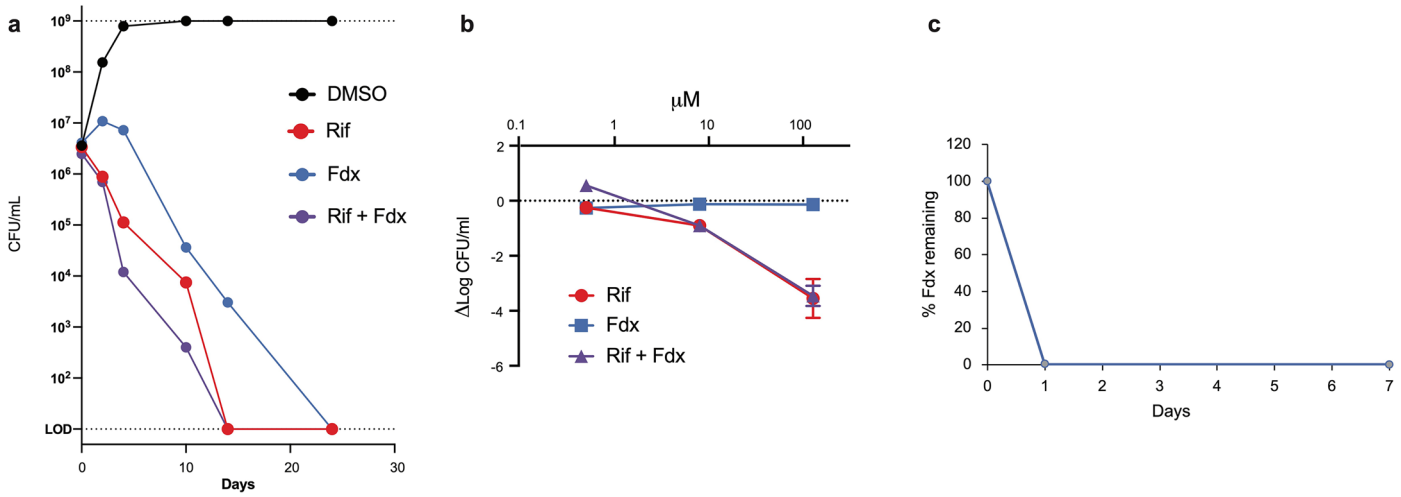

Extended Data Fig. 6 | Fidaxomicin (Fdx) enhances killing of rifampicin (Rif) in culture but not in caseum. a, Time-kill assay showing the effects of DMSO (control), Fdx monotherapy (2× WT MIC_{90} = 749 nM), Rif monotherapy (20× WT MIC_{90} = 243 nM), and the combination of Rif (20× WT MIC_{90} = 243 nM) with Fdx (2× WT MIC_{90} = 749 nM) on WT *Mtb* c.f.u. ml^{-1} over 24 days. Data represent mean ± s.d. (n = 2 biological replicates). **b**, Bactericidal activity of Fdx, Rif, and their combination in the *ex vivo* rabbit caseum model. Log-fold change in c.f.u. ml^{-1} relative to the vehicle control is shown. Data represent mean ± s.d. (n = 3 experimental replicates). **c**, Stability of Fdx (% of the compound remaining) in rabbit caseum homogenate assessed over 7 days.

nature portfolio

Corresponding author(s): Elizabeth Campbell

Last updated by author(s): 10/12/2025

Reporting Summary

Nature Portfolio wishes to improve the reproducibility of the work that we publish. This form provides structure for consistency and transparency in reporting. For further information on Nature Portfolio policies, see our Editorial Policies and the Editorial Policy Checklist.

Statistics

For all statistical analyses, confirm that the following items are present in the figure legend, table legend, main text, or Methods section.

n/a	Confirmed	
☐	☒	The exact sample size (*n*) for each experimental group/condition, given as a discrete number and unit of measurement
☒	☐	A statement on whether measurements were taken from distinct samples or whether the same sample was measured repeatedly
☐	☒	The statistical test(s) used AND whether they are one- or two-sided *Only common tests should be described solely by name; describe more complex techniques in the Methods section.*
☒	☐	A description of all covariates tested
☒	☐	A description of any assumptions or corrections, such as tests of normality and adjustment for multiple comparisons
☐	☒	A full description of the statistical parameters including central tendency (e.g. means) or other basic estimates (e.g. regression coefficient) AND variation (e.g. standard deviation) or associated estimates of uncertainty (e.g. confidence intervals)
☐	☒	For null hypothesis testing, the test statistic (e.g. *F*, *t*, *r*) with confidence intervals, effect sizes, degrees of freedom and *P* value noted *Give P values as exact values whenever suitable.*
☒	☐	For Bayesian analysis, information on the choice of priors and Markov chain Monte Carlo settings
☒	☐	For hierarchical and complex designs, identification of the appropriate level for tests and full reporting of outcomes
☒	☐	Estimates of effect sizes (e.g. Cohen's *d*, Pearson's *r*), indicating how they were calculated

Our web collection on statistics for biologists contains articles on many of the points above.

Software and code

Policy information about availability of computer code

Data collection	SerialEM (ref. 87)
Data analysis	Structural biology software was accessed through the SBGrid consortium (ref.96) and visualizations done in PyMOL (The PyMOL Molecular Graphics System, Version 3.03 Schrödinger, LLC) Statistics were done using Prism 10.4.1 (GraphPad Software, Inc.) MotionCor2 (ref. 88) CryoSPARC v4 (ref. 89) RELION (ref. 90,91) Bsoft package (ref. 102) LIGPLOT (ref. 53) Phenix (ref. 105) Chimera (ref. 93) COOT (ref. 94) webSalvador (ref. 61) Synergyfinder plus (ref. 66)

For manuscripts utilizing custom algorithms or software that are central to the research but not yet described in published literature, software must be made available to editors and reviewers. We strongly encourage code deposition in a community repository (e.g. GitHub). See the Nature Portfolio guidelines for submitting code & software for further information.

Data

Policy information about availability of data

All manuscripts must include a data availability statement. This statement should provide the following information, where applicable:

- Accession codes, unique identifiers, or web links for publicly available datasets
- A description of any restrictions on data availability
- For clinical datasets or third party data, please ensure that the statement adheres to our policy

Data availability. All unique/stable reagents generated in this study are available without restriction from the lead contact, Elizabeth Campbell (campbee@rockefeller.edu). The cryo-EM density maps and atomic coordinates have been deposited in the EMDataBank and Protein Data Bank as follows: MtbEC AAP-SO2 (EMD-48561 and PDB 9MRQ). The atomic models used for initial model building and analysis are available from the Protein Data Bank under the accession codes PDB ID: 8E95.

Research involving human participants, their data, or biological material

Policy information about studies with human participants or human data. See also policy information about sex, gender (identity/presentation), and sexual orientation and race, ethnicity and racism.

Reporting on sex and gender	n/a
Reporting on race, ethnicity, or other socially relevant groupings	n/a
Population characteristics	n/a
Recruitment	n/a
Ethics oversight	n/a

Note that full information on the approval of the study protocol must also be provided in the manuscript.

Field-specific reporting

Please select the one below that is the best fit for your research. If you are not sure, read the appropriate sections before making your selection.

☒ Life sciences ☐ Behavioural & social sciences ☐ Ecological, evolutionary & environmental sciences

For a reference copy of the document with all sections, see nature.com/documents/nr-reporting-summary-flat.pdf

Life sciences study design

All studies must disclose on these points even when the disclosure is negative.

Sample size	n/a
Data exclusions	n/a
Replication	n/a
Randomization	n/a
Blinding	n/a

Reporting for specific materials, systems and methods

We require information from authors about some types of materials, experimental systems and methods used in many studies. Here, indicate whether each material, system or method listed is relevant to your study. If you are not sure if a list item applies to your research, read the appropriate section before selecting a response.

Materials & experimental systems

n/a	Involved in the study
☒	☐ Antibodies
☒	☐ Eukaryotic cell lines
☒	☐ Palaeontology and archaeology
☐	☒ Animals and other organisms
☒	☐ Clinical data
☒	☐ Dual use research of concern
☒	☐ Plants

Methods

n/a	Involved in the study
☒	☐ ChIP-seq
☒	☐ Flow cytometry
☒	☐ MRI-based neuroimaging

Animals and other research organisms

Policy information about studies involving animals; ARRIVE guidelines recommended for reporting animal research, and Sex and Gender in Research

Laboratory animals	New Zealand White rabbits
Wild animals	The study did not involve wild animals
Reporting on sex	For the purposes of this study, we used caseum specimens that were removed from the pulmonary granulomas of female rabbits (infection and necropsy procedures were appropriately referenced in Methods). The caseum specimen was used under ex vivo conditions (96-well plates) using a referenced protocol, with focus on the phenotype of the resident bacterial population. Given our very specific focus on non-replicating M. tuberculosis bacilli in the necrotic ex vivo tissue specimen, we do not consider any gender factors in this study.
Field-collected samples	The study did not involve field-collected samples.
Ethics oversight	Animal studies were carried out with approval from the Institutional Animal Care and Use Committees of the National Institute of Allergy and Infection Disease, NIH, MD (protocol number LCIM-3)

Note that full information on the approval of the study protocol must also be provided in the manuscript.

Plants

Seed stocks	n/a
Novel plant genotypes	n/a
Authentication	n/a